

Seismic modelling and deconvolution of prestack depth migrated images through ray- based Point-Spread Functions



Kristian Jensen

Thesis for the degree of Philosophiae Doctor (PhD)
University of Bergen, Norway
2021

UNIVERSITY OF BERGEN



Seismic modelling and deconvolution of prestack depth migrated images through ray-based Point-Spread Functions

Kristian Jensen



Thesis for the degree of Philosophiae Doctor (PhD)
at the University of Bergen

Date of defense: 15.12.2021

© Copyright Kristian Jensen

The material in this publication is covered by the provisions of the Copyright Act.

Year: 2021

Title: Seismic modelling and deconvolution of prestack depth migrated images through ray-based Point-Spread Functions

Name: Kristian Jensen

Print: Skipnes Kommunikasjon / University of Bergen

Scientific environment

The research presented in this thesis has primarily been conducted in the Geodynamics and Basin Studies research group at Department of Earth Science, University of Bergen, Norway. Parts of the thesis are furthermore based on research carried out at Bureau of Economic Geology, Jackson School of Geosciences, University of Texas at Austin, USA, in Professor Sergey Fomel's research group.

Main supervisor: Associate Professor Isabelle Lecomte, University of Bergen

Co-supervisor: Professor Leiv-Jacob Gelius, University of Oslo

Co-supervisor: Principal Research Geophysicist Tina Kaschwich, NORSAR

Co-supervisor: Professor Børge Arntsen, NTNU

Co-supervisor: Professor Einar Iversen, University of Bergen

In addition to the PhD-funding received directly from the University of Bergen, additional research funds have been provided from the Research Council of Norway (Project #26763 – FOPAK). Additional travel funds have been provided from Fulbright Norway and from The Meltzer Research Fund.

Acknowledgements

I want to first and foremost acknowledge my main supervisor, Isabelle Lecomte, for her outstanding support during my work on this thesis. Her supervision and guidance have been paramount in my development as an independent researcher over these last four years. I would also like to greatly acknowledge my co-supervisors Leiv-Jacob Gelius, Tina Kaschwich, Børge Arntsen and Einar Iversen. All of you have provided invaluable input, guidance, and assistance, and it is due to the contributions from all of you that I have been able to finish this thesis on time.

Although my PhD has been funded by the University of Bergen, I want to acknowledge The Research Council of Norway for additional financial support throughout my PhD. This support has been linked to the FOPAK-project (Forecasting of architecture, seismic characteristics and flow behaviour in paleokarst reservoirs) anchored at NORCE. As such, I would also like to extend my deepest gratitude to Senior Researcher Jan Tveranger at NORCE for including me in the FOPAK-project. I also wish to thank my other collaborators on the FOPAK-project, Bjarte Lønøy, Christos Pennos and Stein Erik Lauritzen, for both their academic input as well as for organizing some truly great social and educational events. Particularly, I appreciate the invitation to join Christos and Bjarte in December of 2018 for field work in the Maaras Cave in Greece.

Furthermore, I wish to extend my sincerest gratitude to Professor Sergey Fomel for inviting me to spend four months at his research group at Bureau of Economic Geology, Jackson School of Geosciences, University of Texas at Austin. In that regard, I also wish to thank Fulbright Norway, The Research Council of Norway (FOPAK-project) and The Meltzer Research Fund, for funding my stay in Texas. The four months I spent there were some of the most rewarding months of my entire PhD, both personally and professionally. It was a true privilege to learn from Professor Fomel, and to feel so welcome in his research group. I would also like to thank Xavier Janson, Harpreet Kaur, Luke Decker, Ray Abma, Ben Gremillion, Melissa Coffman and Gwen Hebert

for collaboration, insightful conversations, and personal support during my time at the Bureau.

Many people at the University of Bergen have also been very helpful in providing suggestions and comments related to the work presented in this thesis. Particularly, I would like to acknowledge Bent Ole Ruud and Henk Keers for their input at various stages of my work. A special thanks also to Paul Lubrano-Lavadera, currently at Ramboll, for providing some of the initial codes that laid the foundation for parts of this project.

Last, but not least, I want to thank my wife Iryn, and my children, Tristan and Katrin, for their continuous love and support during my PhD.

Abstract

Seismic modelling involves simulating the propagation of waves through an Earth model to retrieve information about the subsurface. If an a priori Earth model is known, seismic modelling allows geoscientists to assess how acquisition-, propagation- and processing parameters, may affect the obtained seismic image. Seismic modelling thus remains an important tool in exploration geophysics.

Due to restricted survey illumination, limited bandwidth frequencies and propagation effects in the overburden, seismic images typically yield a blurred and incomplete representation of the actual Earth model parameters. These limited-illumination and blurring effects are expressed through the local point scatterer responses, or *point-spread functions*. When accurately estimated point-spread functions are convolved with an input reflectivity grid, simulated prestack depth migrated images incorporating these effects are obtained. Conversely, if an accurate representation of the inverse point-spread functions can be estimated, seismic images may be deblurred, or deconvolved, to obtain a sharper, higher-resolution representation of the Earth model parameters.

Target-oriented point-spread functions may be estimated via different approaches. Wave-based approaches involve solving the acoustic or elastic wave equation, typically through the implementation of a Finite-Difference, or Finite-Element approach. These approaches are generally robust and accurate, but the computational cost involved may be prohibitive. Alternatively, ray-based approaches may be used. Ray-based approaches involve a high-frequency approximation of the wave equation, which significantly reduces computation time. As such, efficient and flexible estimations of point-spread functions may be obtained at a low computational cost, but inherent limitations in ray theory may lead to less accuracy.

The main objective of this thesis is to further validate, develop and improve a ray-based approach for estimation of point-spread functions. This approach utilizes a transformation which defines the point-spread functions in the wavenumber domain. Such an approach allows for fast computation of point-spread functions, as well as the

possibility for quickly designing analytical point-spread functions tailored to specific needs.

First, an in-depth study of how ray-based point-spread functions compare to wave-based point-spread functions, is presented (Paper 1). The governing equations for both approaches are derived for the homogeneous case, thus allowing for a thorough assessment of the conditions where the two approaches may diverge. Simulated seismic images obtained via point-spread function convolution modelling are also compared to fully modelled and migrated data. The results reveal that both wave- and ray-based approaches accurately model illumination, resolution and amplitude effects observed in the fully migrated images. In addition, although some minor deviations between the wave-based and ray-based approaches are observed, the overall results, as also confirmed through the analysis of the governing equations, indicate that both approaches can be used, even for complex models.

Having validated the potential for ray-based point-spread functions to be used as convolution operators, the next study assesses how well such point-spread functions perform as seismic modelling operators on complex paleokarst geology (Paper 2). Due to the small-scale heterogeneity of paleokarst, wave-based modelling is inherently difficult to perform due to the high computational cost involved. However, precisely because of this small-scale heterogeneity, the ability to accurately simulate how perturbations of model- and seismic parameters affect paleokarst seismic images, is crucial. Through several case studies, different issues and challenges pertaining to seismic characterization and interpretation of paleokarst features are investigated. The validity of the point-spread function convolution approach is confirmed via comparisons with other seismic modelling work previously done on some of the same models.

Finally, the potential of applying ray-based point-spread functions as deconvolution operators on reverse-time migrated images is demonstrated (Paper 3). Ray-based point-spread functions are applied in an iterative conjugate-gradient algorithm for quick estimation of the local inverse Hessian operator valid at a target area of interest. Once

estimated, this operator may be used for target-oriented deconvolution of seismic images. The validity of the approach is assessed through comparisons with results obtained from conventional source-signature deconvolution. The results reveal that the ray-based PSF deconvolution approach yields better resolution gain both vertically and laterally.

List of publications

The following publications are included in this PhD dissertation:

Paper 1: Jensen, K., Lecomte, I., Gelius, L.-J. and Kaschwich, T. (2021). Point-spread function convolution to simulate prestack depth migrated images: A validation study. *Geophysical Prospecting*, pp. 1-20.

Paper 2: Jensen, K., Johansen, M.K., Lecomte, I., Janson, X., Tveranger, J. and Kaschwich, T. (2021). Paleokarst reservoirs: Efficient and flexible characterization using point-spread-function-based convolution modeling. *Interpretation*, 9(2), pp. T331-T347.

Paper 3: Jensen, K., Lecomte, I., Arntsen, B., Wang, T., Kaur, H. and Decker, L. (2021). Deconvolution of reverse-time migrated images via ray-based point-spread functions. (Submitted to *Geophysical Prospecting* in August 2021).

The following additional conference abstracts are also included in the dissertation:

Abstract 1: Jensen, K., Lecomte, I. and Kaschwich, T. (2018). Analyzing PSDM images in complex geology via ray-based PSF convolution modeling. In: *88th SEG Annual International Meeting, Anaheim, CA, USA*, Expanded Abstracts, pp. P3843-3847.

Abstract 2: Jensen, K., Lecomte, I., Janson, X., and Tveranger, J (2020). Efficient and flexible characterization of paleokarst seismic signatures using point-spread function-based convolution modeling. In: *90th SEG Annual International Meeting, Houston, TX, USA*, Expanded Abstracts, pp. 2744-2748.

Other scientific contributions performed during the PhD period, but not included in the dissertation:

Paper: Zhang, R., Li, T., Liu, C., Huang, X., Jensen, K. and Sommer, M. (2021). 3-D joint inversion of gravity and magnetic data using data-space and truncated Gauss-Newton methods. *IEEE Geoscience and Remote Sensing Letters*.

Paper: Johansen, T.A., Ruud, B.O., Tømmerbakke, R. and Jensen, K. (2019). Seismic on floating ice: Data acquisition versus flexural wave noise. *Geophysical Prospecting*, 67(3), pp. 532-549.

Abstract/poster: Lønøy, B., Pennos, C., Tveranger, J., Fikos, I., Vargemezis, G., Jensen, K. and Lauritzen, S.E. (2019). Sediment accumulations in paleokarst reservoirs – Analogues from an active cave system. In: *Bathurst Meeting of Carbonate Sedimentologists 2019*, Palma de Mallorca, Spain.

Abstract/poster: Pennos, C., Christaras, D., Gkarlaouni, C., Jensen, K. and Sotiriadis, Y. (2019). Monitoring earthquake induced CO₂ emissions within a fault-controlled cave. In: *Winter Conference of the Norwegian Geological Society*, Bergen, Norway.

Invited talks:

"Improving simulation of prestack depth migrated seismic images via point-spread function-based convolution modelling." 20-minute presentation given online for internal conference at Jilin University, China. December 2020.

"Point-spread functions in seismic imaging." 30-minute presentation given at Texas Consortium for Computational Seismology Meeting at Bureau of Economic Geology, Jackson School of Geosciences, University of Texas at Austin, November 2019.

Other contributions:

I have assisted three master students (Alma Dzožlic Bradaric, Martin Kyrkjebo Johansen and Thomas Jarle Grimstad) at Department of Earth Science, University of Bergen, with writing computer codes.

Paper 1 is reprinted via the University of Bergen Creative Commons-licence. Paper 2 is reprinted with permission from SEG. All rights reserved. Paper 3 is reprinted with permission from EAGE. All rights reserved. Abstracts 1 and 2 are reprinted with permission from SEG. All rights reserved.

Contents

Scientific environment	3
Acknowledgements	4
Abstract	6
List of publications.....	9
Contents	11
1. Introduction	12
1.1 Seismic modelling	12
1.2 Repeated-1D convolution	15
1.3 Prestack depth migration (PSDM) and the PSF	17
1.4 A ray-based approach for estimating PSFs	21
1.5 PSF convolution modelling	24
1.6 Refinements of the PSF as a convolution operator.....	32
1.7 PSFs as deconvolution operators	37
1.8 Thesis contributions.....	44
2. Conclusions and future perspectives	48
3. Bibliography	52
4. Papers	58
4.1 Paper 1	59
4.2 Paper 2	80
4.3 Paper 3	98
4.4 Abstract 1	139
4.5 Abstract 2	145

1. Introduction

The main objective for this study is to justify the validity of, and investigate potential ways to improve, a seismic modelling approach referred to as point-spread function (PSF) convolution modelling. This chapter provides relevant background information on seismic modelling, PSFs and their applications, as well as a summary of the novel contributions to the field which are presented in subsequent chapters.

1.1 Seismic modelling

Seismic modelling involves the simulation of elastic wave propagation through an Earth model. In exploration geophysics, seismic modelling is an important tool for assessing how acquisition-, propagation- and processing parameters affect seismic images of subsurface environments. Information gathered through seismic modelling may particularly be useful in sensitivity studies performed by seismic interpreters. Seismic modelling is also frequently applied in seismic inversion problems, where alternating modelling and migration algorithms are implemented with the purpose of retrieving the Earth model by minimizing the error misfit function.

Although a substantial variety of seismic modelling methods exist ([Carcione et al., 2002](#)), full-waveform (FW) approaches, which typically involve solving the complete acoustic or elastic wave equation through a discretized Finite-difference (FD) or Finite-Element (FE) implementation, are generally considered the most complete because all types of wave phases are included. A drawback with FW-approaches, however, is that the computational cost involved may be prohibitive. This is particularly problematic for large-scale and elastic 3D studies where small-scale details are to be included, as for, e.g., paleokarst structures, fault zones, magmatic or sand injections, etc. (e.g., [Botter et al., 2014](#); [Botter et al., 2017](#); [Kolyukhin et al., 2017](#); [Eide et al., 2018](#); [Rabbell et al., 2018](#); [Grippa et al., 2019](#); [Wrona et al., 2020](#)). Sensitivity studies where various geological and geophysical parameters are tweaked, adjusted, and assessed multiple times, may also be prohibitive to perform via FW-approaches if new modelling and migration implementations are required after each parameter adjustment.

As an alternative to costly FW-approaches, ray-based (RB) approaches, derived from asymptotic ray theory following a high-frequency approximation of the wave equation, may be implemented. RB-approaches, usually relying either on ray-tracing algorithms or eikonal-equation solvers, allow for efficient and flexible sensitivity studies at a low computational cost, but with potentially less completeness than FW-approaches due to the abovementioned lack of all wave phases. Limitations in RB-approaches include an incomplete wavefield, the requirement of smooth interfaces and smooth velocity fields between these layers, and the risk of inaccuracies due to singular, caustic regions ([Červený et al., 1977](#)). However, refinements to these potential limitations can be made through a composite approach where various ray-based processes are combined ([Gjøystdal et al., 2007](#)).

Regardless of whether a wave- or ray-based approach is applied, the main purpose typically involves solving either a seismic modelling or a seismic inversion problem (Figure 1). Seismic modelling aims to generate synthetic seismic data based on an a priori known Earth model. Seismic inversion, on the other hand, aims to infer the Earth model parameters based on already available seismic data and a specified forward modelling approach. Mathematically, seismic modelling can be expressed via the equation:

$$\mathbf{d} = \mathbf{L}\mathbf{m}, \quad (1)$$

where \mathbf{m} represents the true Earth model parameter (e.g., reflectivity, velocity), \mathbf{L} is a forward modelling operator, and \mathbf{d} the observed seismic data. The inverse problem is formulated as:

$$\mathbf{m} = \mathbf{L}^{-1}\mathbf{d}, \quad (2)$$

where \mathbf{L}^{-1} is a stable approximation of the inverse \mathbf{L} -operator.

Inserting (1) into (2) gives us the following equation:

$$\mathbf{m} = \mathbf{L}^{-1}\mathbf{L}\mathbf{m}. \quad (3)$$

Equation (3) shows that if an accurate inverse L^{-1} -operator is defined, the correct Earth model parameters should be retrieved. Frequently, however, a true inverse modelling operator is challenging to obtain, particularly due to the size of the L -operator. An approximation to the inverse operator thus typically involves applying the adjoint form of the L -operator instead (Schuster and Hu, 2000):

$$\mathbf{m}_{est} = L^T L \mathbf{m}. \quad (4)$$

The $L^T L$ -operator, commonly referred to as the *point-spread function* (PSF), accounts for how frequency bandwidth, overburden propagation effects and limited illumination blur - and possibly remove parts of - the actual Earth model in the seismic image. As such, we only obtain an estimation, \mathbf{m}_{est} , of the true earth model parameter \mathbf{m} .

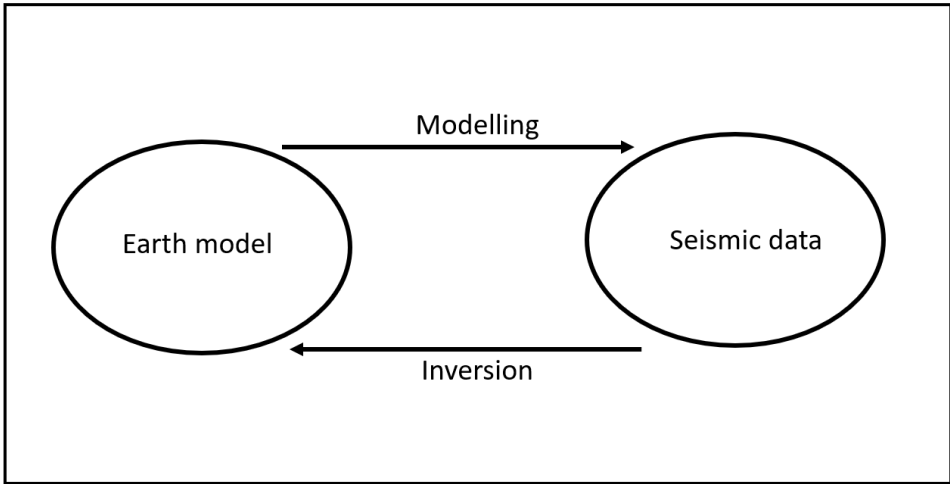


Figure 1: Illustration of seismic modelling and inversion.

Finally, if an inverse approximation of the PSF itself can be obtained, an even more accurate representation of the Earth model \mathbf{m} , may be obtained by multiplying each side of (4) with the inverse $L^T L$ -operator:

$$\mathbf{m} = (L^T L)^{-1} \mathbf{m}_{est} \quad (5)$$

This procedure is commonly referred to as deconvolution, or deblurring, of the seismic image.

Equations (1), (4) and (5) represent the governing equations behind the operations referred to as seismic modelling, migration, and inversion, respectively. As seen in (4) and (5), the key operator in both migration and inversion is the PSF. Accurate estimation of the PSF is therefore essential. The PSF may be computed either through wave-based approaches (e.g., [Xie et al., 2005](#); [Toxopeus et al., 2008](#); [Tang, 2009](#)) or ray-based approaches ([Hamran and Lecomte, 1993](#); [Lecomte and Gelius, 1998](#)). More recently, [Kaur et al. \(2020\)](#) also show how machine learning can be used to estimate the inverse PSF required for inversion.

Before discussing in greater detail the specific properties of the PSF, and how PSFs may be used as seismic modelling and inversion operators, a brief review of one of the simplest methods for forward modelling of seismic images, repeated-1D convolution, will be provided. This method has been widely applied in the industry for decades, and a review of this approach will provide some useful reference examples for this chapter.

1.2 Repeated-1D convolution

In seismic images, vertical (or across-reflector) resolution is traditionally defined as $\lambda/4$, with λ being the wavelength of the applied pulse. Lateral resolution (not necessarily horizontal), on the other hand, is estimated from the Fresnel zone valid at the target of interest. In repeated-1D convolution, a wavelet is convolved trace-by-trace with an input reflectivity grid ([Robinson and Treitel, 1978](#)), thus yielding a modelled seismic image either in 2D (section) or 3D (cube). This approach is a computationally fast method for modelling vertical resolution effects, and, as such, the method remains a popular tool due to the ease in which it may be implemented even on large 3D models. In classical use of 1D convolution, the convolution itself is performed in the (poststack) time-migrated domain ([Lecomte et al., 2015](#)). As this study focuses on simulating prestack depth migrated (PSDM) images, i.e., in the depth migrated domain, we instead use a “depth-equivalent” wavelet for 1D convolution, with this wavelet representing

the time-wavelet stretched in depth. See e.g., [Lecomte et al. \(2016\)](#) for illustration and comparison with PSF-based convolution results.

Figure 2 illustrates the principle of repeated-1D convolution for the simplest case: a single pointwise reflectivity in an otherwise homogeneous model. When convolving this reflectivity model trace-by-trace with an input wavelet, a simulated seismic image is obtained. As the convolution is performed vertically, i.e., equivalent to a zero-offset acquisition over a horizontally-layered media, vertical resolution effects are modelled. Due to the limited bandwidth of the input wavelet, the reflectivity point is now represented as a vertically stretched depth signal corresponding to the input wavelet.

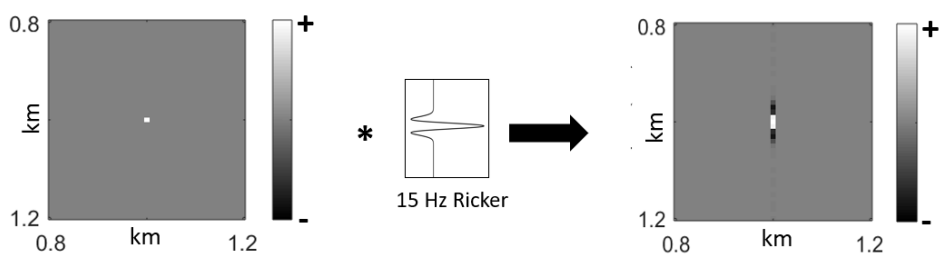


Figure 2: Illustration of repeated-1D convolution where an input reflectivity grid consisting of a single point scatterer is convolved vertically with a wavelet to yield a modelled seismic section. The star symbol represents the convolution operation. Background velocity is defined as $v = 2$ km/s.

The principle of repeated-1D convolution can be extended to more complex geological models, though this is not advisable despite being done a lot ([Lecomte et al., 2015](#)). Figure 3 illustrates the application of repeated-1D convolution in a more complex geological setting characterized by several layers with two steeply dipping faults crossing the layers. This modelling principle is much used for simple and rapid modelling, particularly to add seismic on geomodels derived from either seismic interpretation or outcrop analogues ([Jafarian et al., 2018](#)).

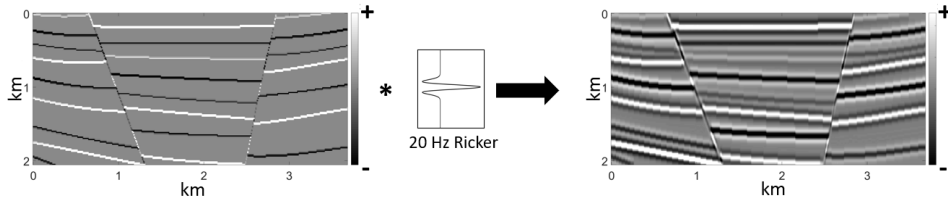


Figure 3: Illustration of repeated-1D convolution for a complex geological setting.

Figure 3 shows how repeated-1D convolution offers a simple way of assessing how a zero-offset acquisition over a complex geological setting would model vertical resolution effects due to the limited bandwidth frequency of the input wavelet. However, while reasonably accounting for such vertical resolution effects, repeated-1D convolution does not account at all for horizontal resolution effects commonly prevalent in 2D and 3D seismic data. Furthermore, by not considering either acquisition geometries or propagation effects in an overburden, limited illumination effects are not accounted for (e.g., the very steep faults in Figure 3 would in practice not appear on actual seismic images). Lateral resolution constraints caused by these effects are not accounted for either.

To better illustrate the limitations inherent in repeated-1D convolution, a more thorough analysis of how blurring and limited illumination impact seismic images, even after migration, will now be provided. This will later allow for a more detailed assessment of how several imaging effects not accurately captured in repeated-1D convolution, will be better preserved via 2(3)D PSF convolution modelling.

1.3 Prestack depth migration (PSDM) and the PSF

Following Equation (4), the PSF-operator is defined based on a matrix multiplication of a selected forward modelling operator, \mathbf{L} , and an approximation of its inverse, \mathbf{L}^T . Following Schuster (2017, p. 116), $\mathbf{L}^T \mathbf{L}$ is the point scatterer response, or PSF, for a single source-receiver pair. When integrating over all source-receiver combinations, data coordinates and frequencies, a PSDM image is then obtained. In the migration

process, \mathbf{L} represents the forward propagating wavefield, and \mathbf{L}^T the backpropagating wavefield.

To illustrate the relationship between PSDM and PSFs, we may consider a homogeneous velocity model of size $2 \text{ km} \times 2 \text{ km}$, sampled at every 0.01 km , with a constant velocity of $v = 2 \text{ km/s}$. The model contains a single point scatterer with a velocity of $v = 2.1 \text{ km/s}$ at the centre point of the model. Four different survey setups were next defined. In all survey setups, sources and receivers are located at depth $z = 0.01 \text{ km}$. All surveys consist of a single shot at $x = 1 \text{ km}$. The first survey consists of one receiver located at $x = 1 \text{ km}$. The second survey consists of three receivers located between $x = 0.5 - 1.5 \text{ km}$, spaced 0.5 km apart. The third survey consists of nineteen receivers located between $x = 0.1 - 1.9 \text{ km}$, spaced 0.1 km apart. The final survey consists of two hundred receivers located between $x = 0.01 - 2 \text{ km}$, spaced 0.01 km apart. The survey setups are illustrated in Figure 4a. For each survey, a zero-phase Ricker wavelet with peak frequency of 15 Hz , sampled at every 1 ms , was used.

Forward modelling was performed for each of the four survey setups using a 2D acoustic Finite-difference (FD) approach with the domain discretized with a 2nd-4th order scheme (second-order in time, and fourth-order in space) based on the numerical implementation outlined in [Youzwishen and Margrave \(1999\)](#). Half-space was added to all edges to avoid unwanted boundary reflections. The obtained seismic traces were next back-propagated using the same FD-approach. Finally, reverse-time migration (RTM) ([Baysal et al., 1983](#)) was performed by cross-correlating all forward-modelled and back-propagated wavefields to obtain the point scatterer response, or PSF. Figure 4 illustrates the obtained results.

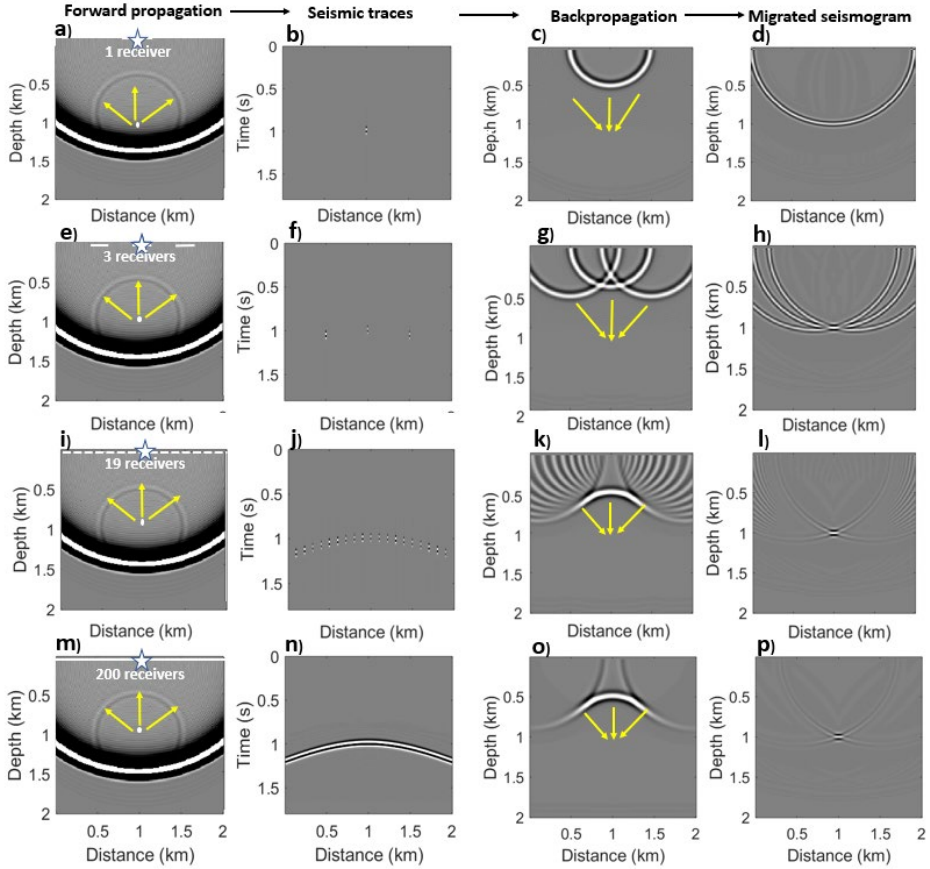


Figure 4: Snapshot of forward-modelled wavefield with the star symbol representing shot position and the dot representing the point scatterer location, obtained seismic traces, snapshot of back-propagated wavefield, and migrated seismogram for a)-d) Survey 1; e)-h) Survey 2; i)-l) Survey 3; m)-p) Survey 4.

The PSFs extracted from all the migrated images using a window of size 0.4 km times 0.4 km (41×41 grid points), and their corresponding wavenumber spectra, are illustrated in Figure 5. The extracted PSFs are here all normalized to have the same amplitude range.

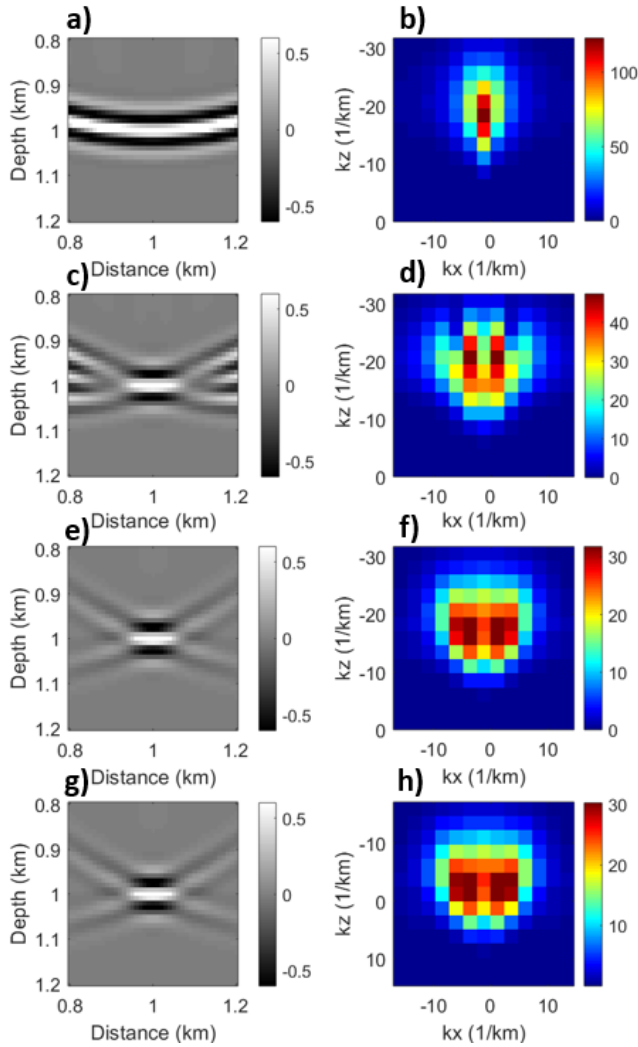


Figure 5: PSFs and corresponding wavenumber spectra for a)-b) PSF extracted from Fig. 4d; c)-d) PSF extracted from Figure 4h; e)-f) PSF extracted from Figure 4l; g)-h) PSF extracted from Figure 4p.

When increasing the number of shot-receiver combinations, more constructive interference between the forward-propagated and back-propagated wavefronts is obtained at the point scatterer location (Figure 5a, 5c, 5e, 5g). As such, an increase in shot-receiver combinations results in a more accurate representation of the point scatterer. However, due to limitations in survey illumination (because of limited

aperture and surface location only) and frequency bandwidth, the resulting PSFs nevertheless, even after constructive interference, do not fully image what is supposed to be just a single point scatterer occupying one grid cell. This illustrates how the parameters inherent in the $L^T L$ -operator blur the point scatterer in the PSDM image. The corresponding wavenumber spectra (Figure [5b](#), [5d](#), [5f](#) and [5h](#)) reflect this further, where an increase in shot-receiver combinations yields greater coverage in the wavenumber domain. The results presented in Figure [5](#) also exemplify how greater coverage in the wavenumber domain yields greater resolution in the spatial domain, which is a familiar concept in signal theory.

It should finally be noted that although a wave-based implementation was used in this example (RTM), the estimation of the point scatterer responses could also be computed via a Kirchhoff approach (see e.g., Fig. 6 in [Lecomte, 2008](#)). In such an approach, the amplitude recorded at the total scattering traveltime $t = t_s + t_r$, with t_s representing the traveltime between source point and point scatterer, and t_r representing the traveltime between the point scatterer and receiver, would automatically be mapped and smeared along an ellipse (or circle in the case of a zero-offset source-receiver setup, as seen in Fig. [4a](#)) in the spatial domain, representing all possible locations that would yield the obtained amplitude value at t . Constructive and destructive interference between all ellipses (circles) resulting from each shot-receiver combination would then yield the PSF, similarly to any wave-based migration.

1.4 A ray-based approach for estimating PSFs

The procedure illustrated in the previous subsection for estimating PSFs may be applied to any model, including complex, inhomogeneous geological models. If the velocity model is familiar, the true velocity model is usually applied for estimating the forward modelled Green's functions, while a smooth migration velocity model is generally applied for estimating the back-propagation ([Xie et al, 2005](#)). The Green's functions may either be estimated directly via this approach ([Xie et al., 2005](#)), or, alternatively, the velocity and/or density value may be perturbed at a single point in the

smooth model followed by forward modelling and migration. The point scatterer response may then be extracted as the PSF ([Cao, 2013](#)).

Both approaches, while robust, typically require a substantial computational effort, particularly for large 3D models. Following [Hamran and Lecomte \(1993\)](#), [Lecomte and Gelius \(1998\)](#) and [Gelius et al. \(2002a\)](#), an alternative approach for estimating the PSFs in inhomogeneous models involves the use of ray-based information to define the PSF as a collection of so-called *scattering wavenumber vectors* ([Lecomte, 2008](#)) in the wavenumber domain. Understanding resolution in seismic migration is indeed easier when visualizing illumination in the wavenumber domain ([Beylkin et al., 1985](#)). The entire collection of scattering wavenumber vectors yields the wavenumber domain representation of the PSF, and once this is estimated, an inverse Fourier transform may be applied to obtain the PSF in the spatial domain.

For estimation of the PSF via this approach, a target point is first defined, and any ray tracing ([Červený et al., 1977](#)), wavefront construction method ([Vinje et al., 1993](#)) or eikonal solver ([Podvin and Lecomte, 1991](#)), may then be applied in a smooth input velocity model (migration of actual seismic data uses such smooth velocity models as first estimated from the data in various manners) to calculate Green's functions between survey positions, i.e., shots and receivers, and the target point (Figure [6a](#)). The incident and scattered slowness vectors (\mathbf{p}_S and \mathbf{p}_R) are then computed for each shot-receiver combination at the target point, being the key parameters of the ray-based PSF under a local plane-wave assumption (Fig. [6a](#); [Lecomte, 2008](#)). Alternatively, a local parabolic-wave assumption could also be used ([Gelius et al., 2002b](#)). For all shot-receiver combinations, the so-called *illumination vectors*, defined by $\mathbf{I}_{SR} = \mathbf{p}_R - \mathbf{p}_S$, are computed (Fig. [6b](#)). Finally, the wavelet spectrum is mapped along each illumination vector, thus yielding the sought-after scattering wavenumber vectors (Fig. [6c](#)). The collection of scattering wavenumber vectors, often referred to as a *PSDM filter*, now represents the PSF in the wavenumber domain, and once an inverse Fourier transform is applied, the PSF is obtained in the spatial domain (Fig. [6d](#)).

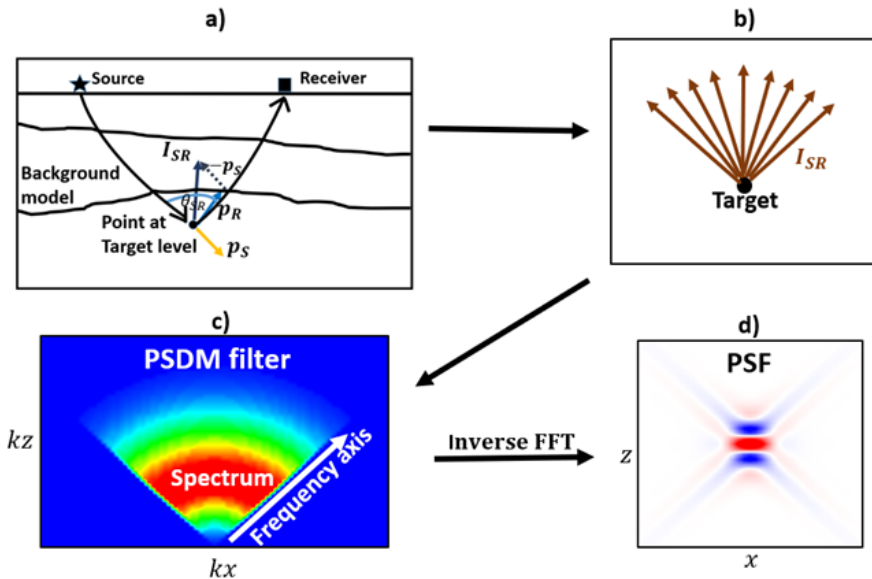


Figure 6: Procedure for estimating PSFs via ray-based approach. a) Ray tracing is used to estimate the illumination vector (I_{SR}) for a single shot at a target point. b) All illumination vectors for a complete survey are obtained. c) Illumination vectors are combined with the wavelet frequency spectrum to obtain the local PSDM filter. d) The PSF is obtained in the space ($x - z$) domain via an inverse Fourier transform. Figure obtained from Jensen et al. (2021b).

The approach illustrated in Figure 6 offers a cheap, efficient and flexible alternative to full-waveform approaches. However, as already pointed out, certain inherent limitations in ray-based approaches may result in slight inaccuracies. [Jensen et al. \(2021b\)](#) (Paper 1 in this thesis) illustrate how the plane-wave assumption, and the far-field approximation used for ray-based approaches, may result in some divergence between ray-based and wave-based PSFs, especially for target points close to the shot location. Nevertheless, most scenarios resulting in a noticeable divergence between the two approaches would occur in unrealistic geological settings such as shallow targets characterized by high velocity and low frequencies ([Jensen et al., 2021b](#)).

1.5 PSF convolution modelling

A PSDM-image can, ultimately, be viewed as the image resulting from the interference of all PSFs obtained at each grid point in the applied model. In the spatial domain, Equation (4) may be expressed as a convolution operation between the input reflectivity grid, \mathbf{m} , and the PSFs, $L^T L$:

$$\mathbf{m}_{est} = L^T L * \mathbf{m}. \quad (6)$$

To illustrate this, we consider again the PSF generated from the survey setup in Figure 4m. We now gradually add more point scatterers horizontally on each side of the central grid point, and convolve the reflectivity grids with the PSF. We then obtain the results illustrated in Figure 7.

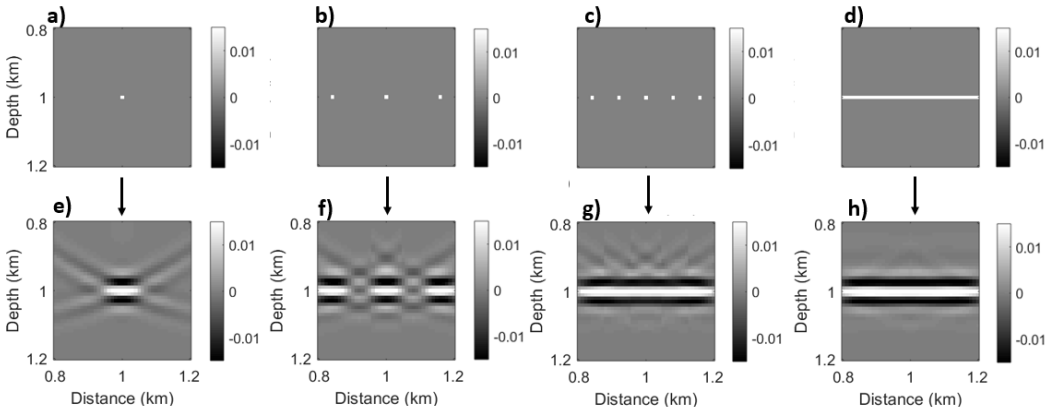


Figure 7: (a-d) Input reflectivity grids. (e-h) Corresponding simulated PSDM-images obtained after convolution with the PSF estimated from Survey 4 in Figure 4.

In this example, it is assumed that the PSF computed at the centre point is valid throughout the target area. In practice, minor deviations should be expected at different points within the target area, but for smaller targets in geologically simple models, these deviations are generally negligible (Jensen et al., 2021b). The convolution of an

input reflectivity grid, represented by \mathbf{m} , and a computed PSF, represented by $\mathbf{L}^T\mathbf{L}$, thus allows for simulation of PSDM-images incorporating effects caused by, e.g., limited bandwidth, illumination, etc. (Lecomte et al., 2003; Lecomte, 2008; Toxopeus et al., 2003; Toxopeus et al., 2008). Realistic PSDM seismic images, can then be modelled, even for complex geomodels (Lecomte et al., 2003; Lecomte et al., 2016).

Furthermore, in contrast to repeated-1D convolution, PSF convolution modelling accounts for both vertical *and* lateral resolution effects. This can now be seen by comparing Figure 2 and Figure 7e, where the same input reflectivity grid has been applied for both cases. Observe how in Figure 7e, the point scatterer is smeared not only vertically, but horizontally as well, thus illustrating how PSF convolution modelling yields a more realistic representation of what we may expect a PSDM-image to look like. This is confirmed by comparing Figures 2 and 7e to the actual migrated point scatterer illustrated in Figure 5g.

The local across-reflector resolution may, mathematically, be estimated based on the magnitude of each illumination vector in the wavenumber domain. This magnitude is a function of the opening angle, θ_{SR} , between the incident and scattered illumination vectors (Figure 6a), and the velocity, v , of the incident and scattered waves at the image point (Lecomte, 2008):

$$\mathbf{I}_{SR} = \frac{2 \cos\left(\frac{\theta_{SR}}{2}\right)}{v} \mathbf{u}_{SR}, \quad (7)$$

Here \mathbf{u}_{SR} is a unit vector pointing in the direction of \mathbf{I}_{SR} . From (7) we may infer that a wide angle between the incident and scattered illumination vectors, and/or high velocity at the target point of interest, will result in poor resolution.

In addition to accounting for vertical and lateral resolution effects, PSF convolution modelling also accounts for limited illumination of target areas. The fan of scattering illumination/wavenumber vectors (Figure 6b-6c) is indeed indicative of the geological dip-range which is illuminated at the target point. As proven mathematically in Gelius

[et al. \(2002a\)](#), any reflector *perpendicular* to an illumination vector will be imaged well, whereas any reflector *not* having a perpendicular illumination vector will not be imaged well (Figure 8). In PSDM-images, this is often manifested in geology containing, for instance, steeply dipping faults. As illustrated in Figure 9, a symmetrical PSF defined via a PSDM-filter with maximum dip range of 45° in both directions away from the vertical illumination vector, will fail to image faults dipping at a greater angle than this. The faults dipping with 0° (a), 15° (b) and 45° (c) are imaged well after PSF convolution modelling, but the fault dipping with 75° (d) is not imaged well. As such, PSF convolution modelling can be an efficient tool for modelling whether or not a specific survey setup applied over a specific velocity model will capture the geological features at a target area. This information is not possible to assess at all with repeated-1D convolution, in addition to the missing lateral resolution effect (the latter also constrained by the illumination). In Figure 10a, repeated-1D convolution with a 20-Hz Ricker wavelet vertically across a specific target area will image all geological features shown in the reflectivity grid. Assuming next that a chosen survey setup and background model would yield an asymmetric PSF with a dip range between -15° and $+45^\circ$, there would be no illumination vector perpendicular to the fault seen in the reflectivity grid, Figure 10b shows how 2D PSF convolution modelling with this PSF would properly yield a seismic image where the fault is not captured. Such illumination effects are crucial to assess in seismic mapping of, e.g., faults and fault zones and any steep geological features (salt flanks, intrusions, folds, etc).

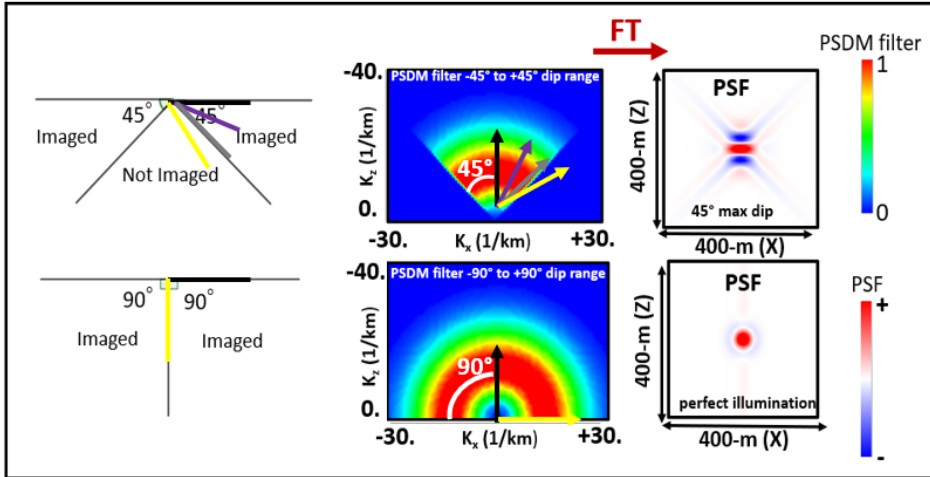


Figure 8: Illustration of dip ranges which may be imaged from a PSDM filter defined with an illumination range of a) -45° to $+45^\circ$ and b) -90° to $+90^\circ$. The lines perpendicular to the vectors in the PSDM filter represent the dip angle imaged by each vector.

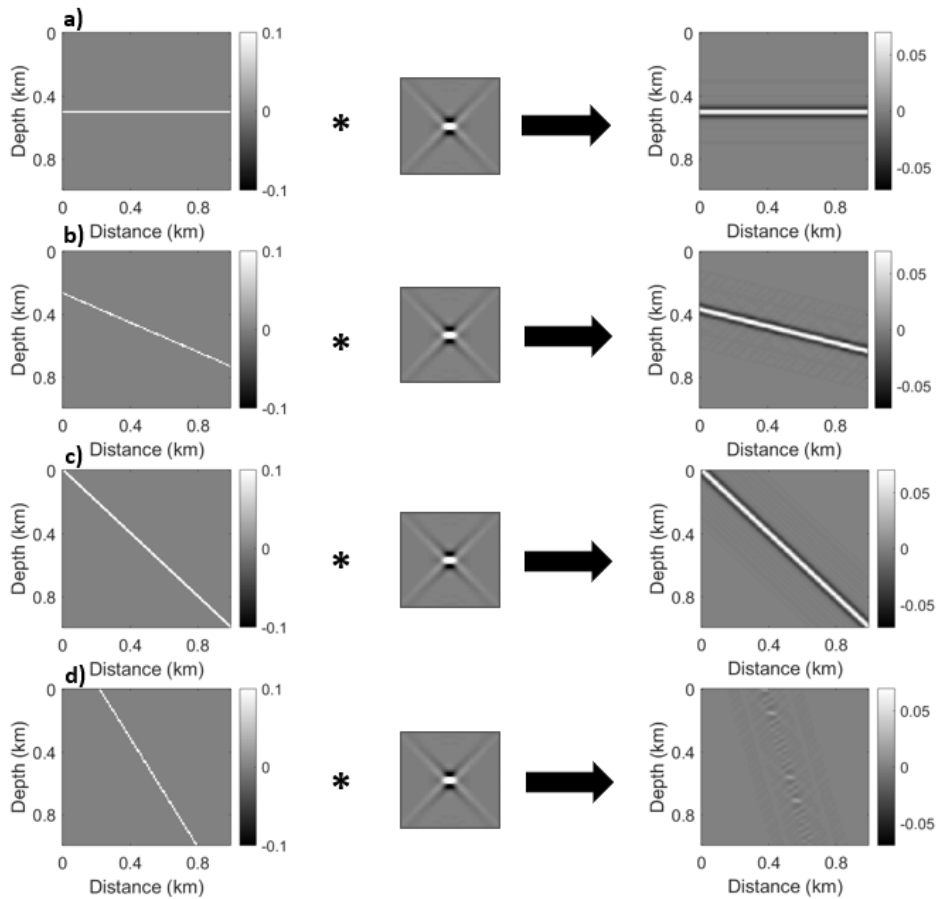


Figure 9: Convolution of input reflectivity grids and a PSF defined with a maximum dip of 45° away from the vertical illumination vector, 15 Hz peak frequency, and in a background velocity of 2 km/s. The reflectivity grids consist of a fault dipping with a) 0° , b) 15° , c) 45° and d) 75° , respectively.

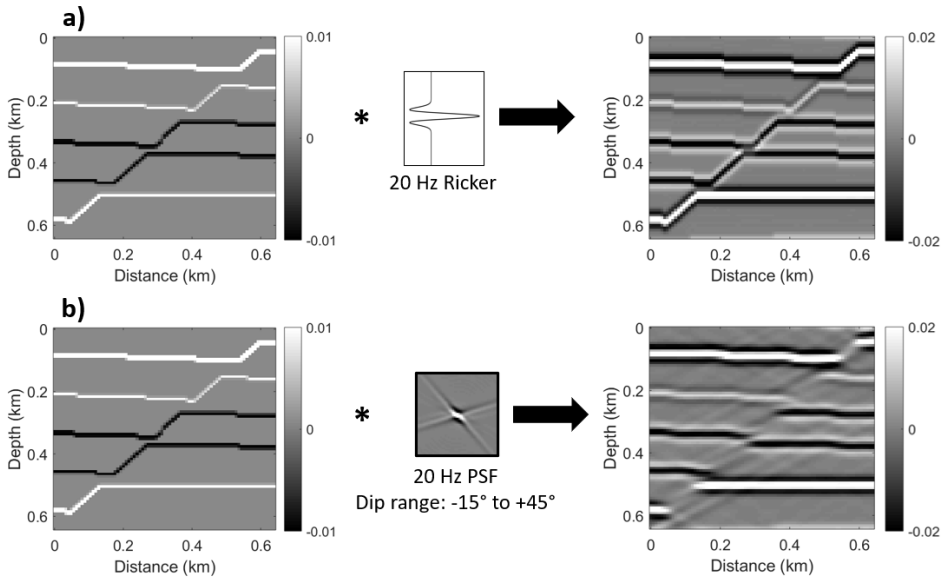


Figure 10: a) Repeated-1D convolution of input reflectivity grid with 20-Hz Ricker wavelet. b) 2D PSF convolution of the same input reflectivity grid with a PSF unable to image the fault feature in the geological model due to limited dip range.

Finally, it should be emphasized that the concept of convolution modelling is also extendable to complex 3D geomodels (e.g., [Lecomte et al., 2015](#); [Lecomte et al., 2016](#); [Rabbel et al., 2019](#); [Wrona et al., 2020](#); [Jensen et al., 2021a](#)). To illustrate this concept, a 3D velocity model of the Guilin Karst Tower system in China ([Janson and Fomel, 2011](#)), with a highlighted target cube, is illustrated in Figure 11. For the given target cube, repeated-1D convolution was performed. PSF-based convolution modelling was next performed using an analytically defined PSF with a maximum dip of 45° as a proxy for standard 3D seismic. To further highlight the impact of illumination and resolution effects in PSDM images, PSF-based convolution modelling was also performed using a PSF with a maximum dip of 20°. This latter PSF represents a typical dip range obtained if the target area lies beneath complex overburden structures, such as salt bodies, or if a thin high-velocity layer is present above the target ([Eide et al., 2018](#)). The two dip ranges furthermore represent typical values obtained from wide-azimuth and narrow-azimuth acquisition ([Feng et al., 2012](#); [Wang et al., 2019](#)). A 30-Hz Ricker wavelet was used for both repeated-1D convolution and PSF convolution

modelling, and the background velocity was set to 3.5 km/s based on average P-velocity values for the target area. The seismic results obtained for a vertical section (XZ-plane) is illustrated in Figure 12, while Figure 13 illustrates the results obtained for a horizontal slice (XY-plane).

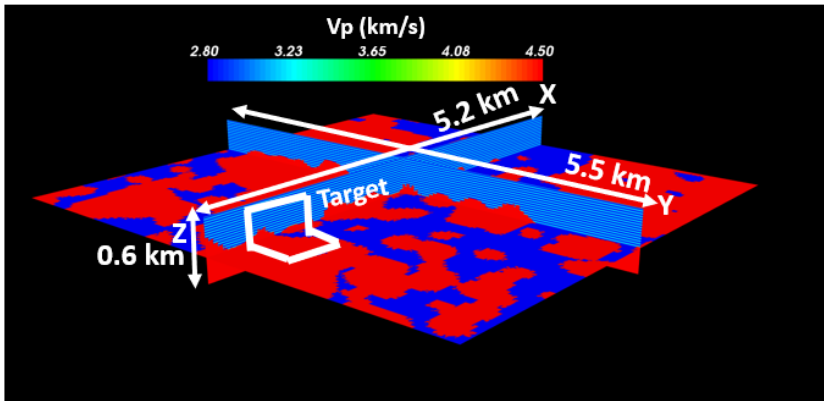


Figure 11: P-velocity model of the Guilin Karst Tower system with selected target area highlighted.

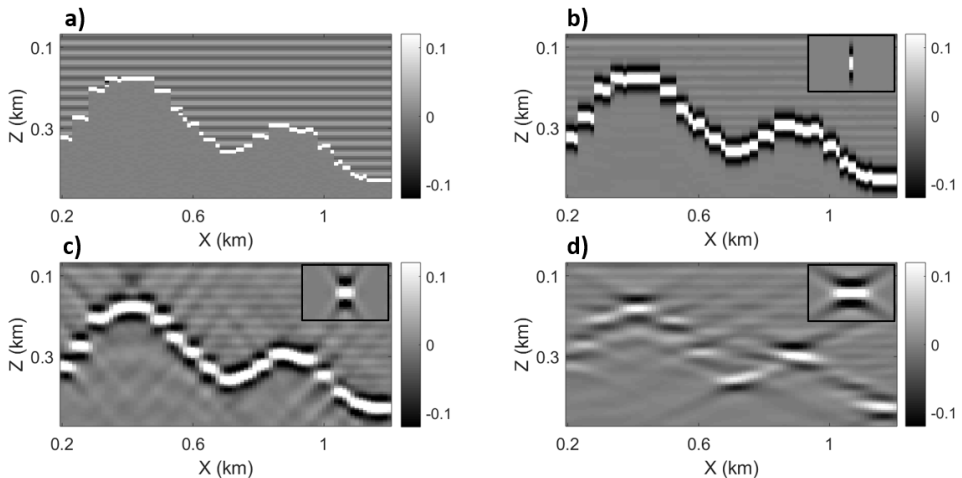


Figure 12: Seismic data obtained via repeated-1D convolution and 3D PSF convolution modelling in the XZ-plane at the target defined in Figure 11 with superimposed PSFs scaled to model. a) Input reflectivity grid; b) repeated-1D convolution result; c) 3D PSF convolution result with maximum illumination dip of 45°; d) 3D PSF convolution result with maximum illumination dip of 20°.

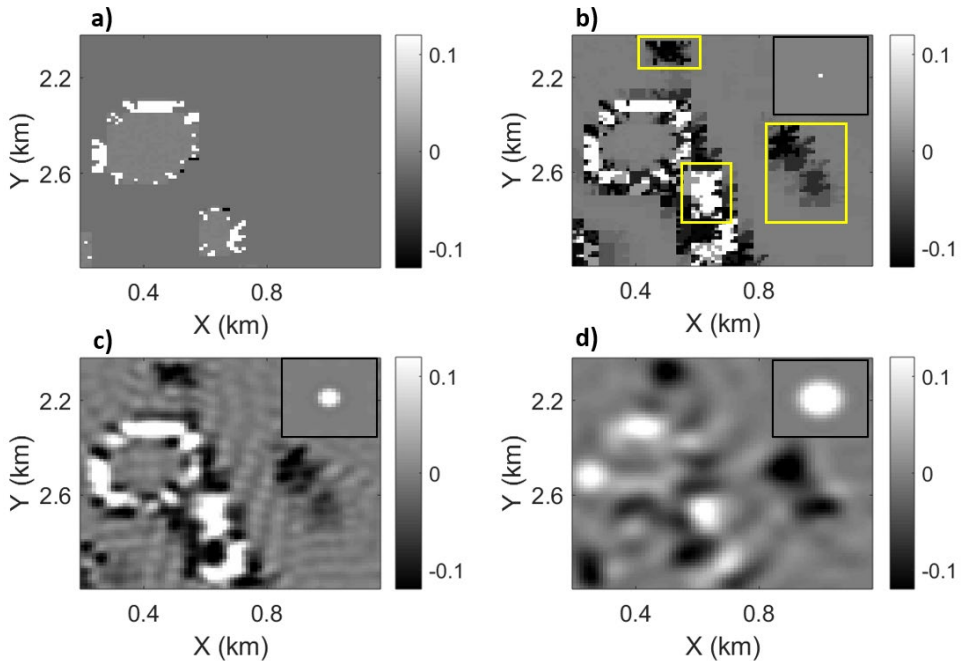


Figure 13: Seismic data obtained via repeated-1D convolution and 3D PSF convolution modelling in the XY-plane at the target defined in Figure 11 with superimposed PSFs scaled to model. a) Input reflectivity grid; b) repeated-1D convolution result; c) 3D PSF convolution result with maximum illumination dip of 45°; d) 3D PSF convolution result with maximum illumination dip of 20°.

The repeated-1D convolution results capture vertical resolution effects caused by limited frequency bandwidth, as evident at the main reflector which represents the top of the karst-tower system (Figure 12b). Furthermore, and still due to vertical resolution effects from band-limited frequency, seismic signals appear even in parts of the image where there is no reflectivity (Figure 13b, yellow boxes). This results from the sole vertical smearing of structures located either above or below the selected depth (Z) slice. The same phenomenon is observed in the seismic images obtained after PSF convolution modelling (Figure 12c-12d, 13c-13d), as expected.

The main difference between the repeated-1D convolved results and the PSF-convolved ones is the total failure of repeated-1D convolution to account for proper horizontal resolution effects. In the vertical section (XZ-plane; Figure 12), the main reflector is indeed more smeared horizontally when a PSF with maximum dip of 45° is applied (Figure 12c). This is further evident in the horizontal slice (XY-plane, Figure 13), where many small-scale features captured by repeated-1D convolution are not resolved in practice, as correctly modelled with PSF convolution (Figure 13c). When applying a PSF with a maximum illuminated dip of 20° , the problems are exacerbated because the lateral resolution further degrades due to a narrower illumination pattern. In addition, illumination contained in the PSF-operator in that case prevents the steep parts of the karst-tower system to be imaged (Figure 12d). Only the horizontal peaks and valleys of the tower system are captured. As a result, the seismic images obtained for both the XZ-plane (Figure 12d) and the XY-plane (Figure 13d) are difficult to interpret. The presence of, e.g., a high-velocity layer above the karst tower, yielding such strong illumination limitations, would therefore severely impact the geological interpretation of the karst tower features from seismic data. PSF convolution modelling thus allows for a more proper assessment of how various parameters may affect illumination and resolution in PSDM-images that what conventional repeated-1D convolution allows, especially for complex (non-flat) 3D geomodels.

1.6 Refinements of the PSF as a convolution operator

Having outlined the main principles of how PSFs may be used as convolutional operators for accurate simulation of PSDM-images, I will now briefly discuss two areas of refinement which may be considered when designing PSFs. First, I will highlight how geometrical spreading effects in complex models may yield different PSFs at the same target area depending on the chosen amplitude adjustments. Next, I will illustrate how PSFs may be defined for modelling different imaging conditions in PSDM.

As a wave propagates through the Earth, its energy decays with increasing distance from the source due to geometrical spreading, scattering (reflection, transmission, diffraction and conversion) and attenuation. High velocity bodies particularly cause

divergence of the wavefront and an even more rapid decay in amplitudes with distance. The loss of energy may be compensated for by multiplying the wavefield by a scaling function. A perfect recovery of amplitudes so that they accurately relate to reflectivity values yields a so-called *true-amplitude* mode (Gray, 1997). Correspondingly, if no scaling is applied whatsoever to the seismic data, the resulting seismic image may be characterized as representing a *raw-amplitude* mode. The true-amplitude mode may, in the context of PSF convolution modelling, be considered as the PSF resulting from equally-weighted illumination vectors, while the various amplitude corrections attempted in real cases will yield a non-uniform weighting of these, often resulting in lower weight for the illumination vectors attached to longer raypaths, thus further reducing lateral resolution.

As illustrated in Jensen et al. (2018), several geological features may not be imaged properly if amplitude loss is not accurately compensated for. To illustrate this, a selected target area of the Sigsbee2A P-velocity model (Paffenholz et al., 2002) is selected (Figure 14). Using a zero-phase 20-Hz Ricker wavelet, the standard marine-survey parameters for the Sigsbee2A-model were implemented. Two PSFs were then estimated at the centre of the target area: one modelled after a true-amplitude mode, and one modelled after a raw-amplitude mode. The results obtained after PSF convolution modelling with the input reflectivity grid are displayed in Figure 15.

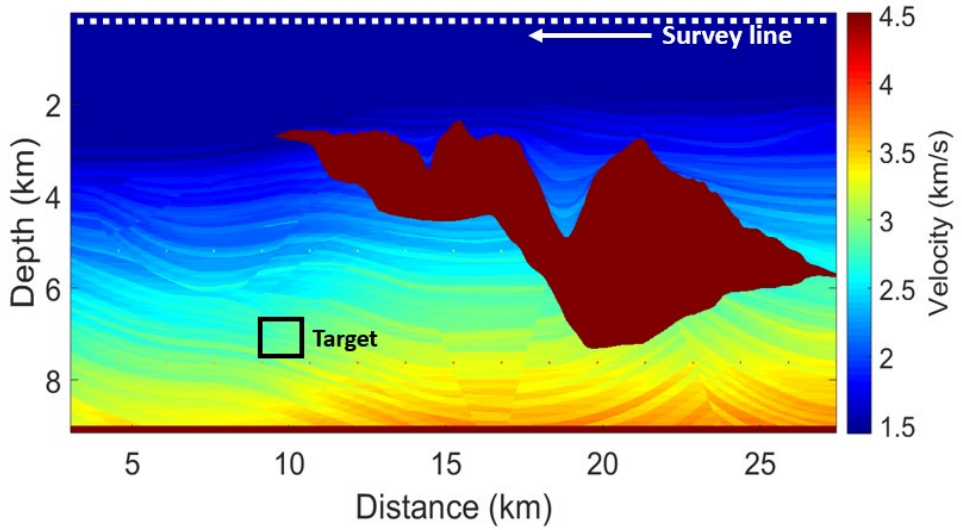


Figure 14: The Sigsbee2A P-velocity model with a selected target area highlighted.

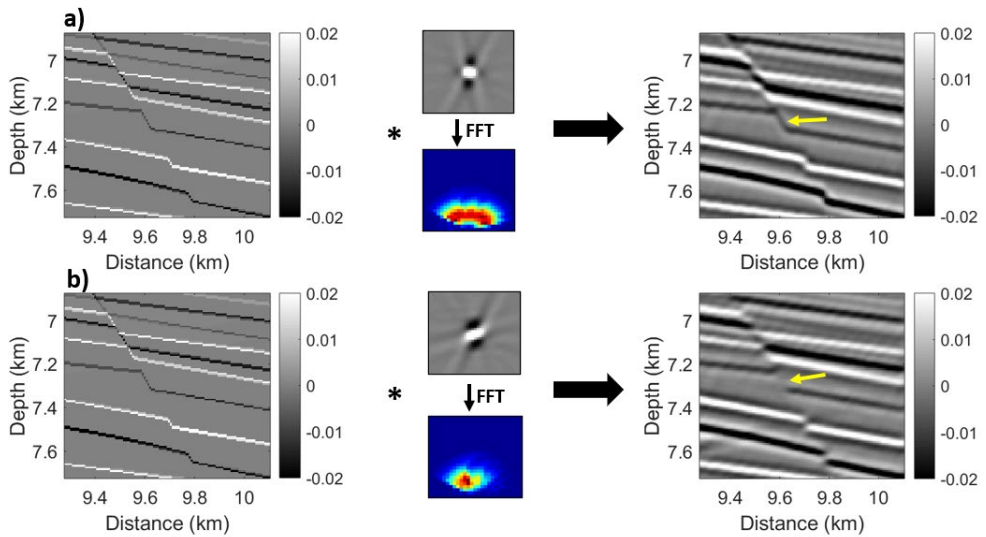


Figure 15: PSF convolution modelling within the target area of Figure 14, with PSF defined at the centre of the target from either a) true-amplitude mode, or b) raw-amplitude mode.

The fault (marked with the yellow arrow) is imaged when the PSF is designed according to a true-amplitude mode (Figure 15a). However, when a raw-amplitude PSF is applied, the fault is not imaged (Figure 15b). By considering the wavenumber spectra of the two PSFs, also illustrated in Figure 15, the illuminated dip range remains the same, but parts of the spectra are damped when keeping raw amplitudes. The illumination vector perpendicular to the fault is strongly weakened in the wavenumber spectrum. For this target, a seismic interpreter may still, however, be able to infer the presence of a fault in the seismic section, as the surrounding geological layers are imaged, the fault thus appearing – as often – as a discontinuity. Nevertheless, the example illustrates that the way the amplitude effects are accounted for could influence the PSF-operator, and subsequently the seismic image. More illustrative examples of this phenomenon are presented in [Jensen et al. \(2018\)](#).

Another aspect which may affect the resolution of the PSF-operator involves the specific imaging condition which is to be simulated. For a Kirchhoff-type imaging condition, the absolute value of the wavelet spectrum, $|S(\omega)|$ (ω representing angular frequency), is typically applied in the governing imaging equation ([Gelius et al, 2002a](#)). However, for a two-way wave-equation migrated image using, e.g., a cross-correlation imaging condition ([Claerbout, 1971](#)), as in RTM, the wave spectrum is multiplied by its complex conjugate in the frequency domain. We then obtain a factor of $|S(\omega)|^2$ in the imaging equation. The $|S(\omega)|^2$ -factor should therefore, if such an imaging condition is desired, be mapped along the illumination vectors in Figure 6c instead of the $|S(\omega)|$ -factor. This may however affect the coverage in the wavenumber domain and, as such, the resolution.

To illustrate the difference between the two imaging conditions, we consider again the survey setup in Figure 4m. Ray-based PSFs valid for the target were generated for both imaging conditions. The PSFs with their respective wavenumber spectra, as well as the extracted vertical and horizontal centre traces, are illustrated in Figure 16.

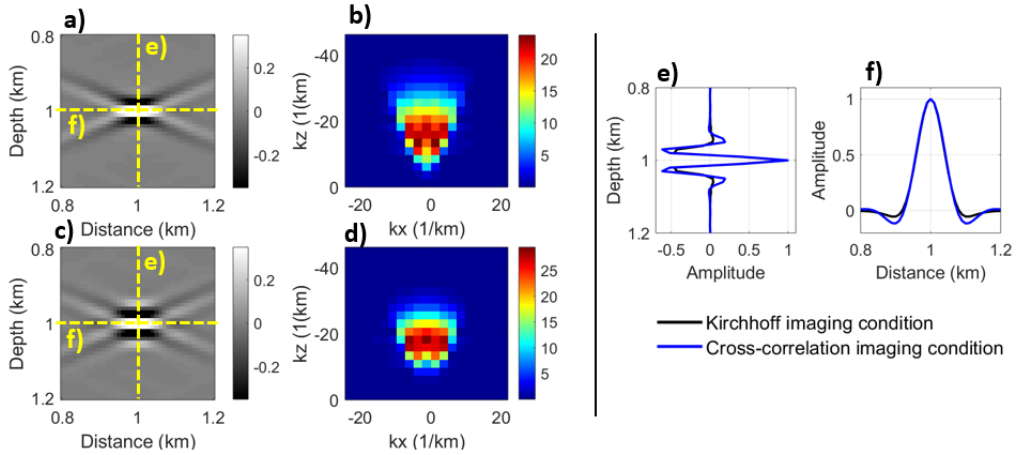


Figure 16: PSFs and corresponding wavenumber spectra computed from (a-b) Kirchhoff imaging condition and (c-d) cross-correlation imaging condition. e) Vertical centre traces. f) Horizontal centre traces.

There are some slight resolution differences between the two PSFs, with the PSF obtained from the Kirchhoff imaging condition yielding slightly better coverage in the wavenumber domain (Figure 16b). The extracted traces across the PSF (16e-16f) further reveal that the wavelet side lobes become slightly more prominent with the cross-correlation imaging condition. To further illustrate the effects resulting from applying the PSFs as convolution operators, both PSFs were convolved with a reflectivity grid consisting of a single reflector (Figure 17). The image obtained from the PSF designed based on a cross-correlation imaging conditions suffers, as expected from the results in Figure 16, from slightly worse resolution. This is exemplified at the locations marked with yellow arrows in Figure 17c. Although these effects may appear minor, they may nevertheless be important to account for, particularly if PSFs are designed as deconvolution operators, where even small deviances from the correct resolution, could result in deconvolved images of low quality.

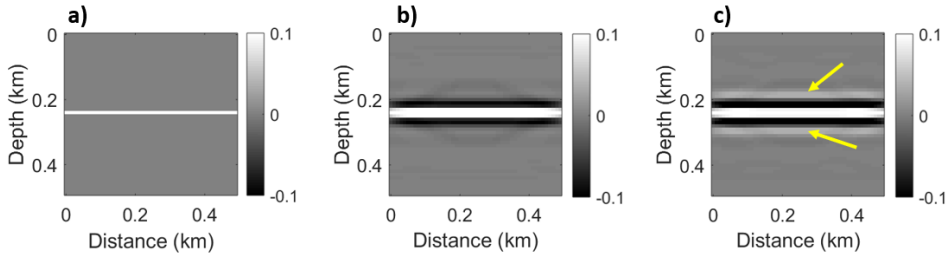


Figure 17: a) Input reflectivity grid. Simulated PSDM-image obtained after convolution with PSF designed from b) Kirchhoff imaging condition and c) cross-correlation imaging condition.

Although this subsection has focused on two potential refinements to include in the design of PSF-operators, other refinements beyond these may also be easily incorporated. Examples include adding anisotropic effects ([Lecomte and Kaschwich, 2008](#)), going from a plane- to a parabolic-wavefront assumption to further improve the PSF for shallow and closer-to-source targets ([Gelius et al., 2002b](#)), the inclusion of converted waves ([Gelius et al., 2002a](#)), and accurate incorporation of Amplitude Versus Offset (AVO)/Amplitude Versus Angle (AVA) effects ([Lecomte, 2008](#)).

1.7 PSFs as deconvolution operators

The previous sections focused on how PSFs, when applied as convolution operators on an input reflectivity grid, may yield a simulated PSDM-image incorporating illumination and resolution effects. When applied to inverse modelling, i.e., when an approximation of the inverse PSF operator is applied on a seismic image to retrieve the input reflectivity grid, the procedure is commonly referred to as deconvolution ([Arya and Holden, 1978](#)) or deblurring ([Schuster and Hu, 2000](#)), expressed mathematically through Equation (5).

Due to the size of the $L^T L$ operator in Equation (5), a true inverse of this operator is usually difficult to obtain for seismic data. Several strategies therefore exist for solving that equation. By linearizing the forward problem in seismic exploration, [Tarantola \(1984\)](#) demonstrates how the inverse solution may be obtained by minimizing the difference between observed and predicated data through an iterative algorithm. An

example of such an approach in seismic migration is least-squares migration (Nemeth et al., 1999) which may be solved in the data domain (e.g., Kuhl and Sacchi, 2003; Dai et al., 2011; Dai et al., 2012; Dai and Schuster, 2013; Xue et al., 2016) or the image domain (e.g., Hu et al., 2001; Rickett, 2003; Guitton, 2004; Valenciano et al., 2006; Yu et al., 2006; Aoki and Schuster, 2009; Tang, 2009; Zhao and Sen, 2018; Jiang and Zhang, 2019, Xu et al., 2020). Data-domain approaches typically involve repeated modelling and migration with the aim of minimizing the error/misfit function between observed and predicted results. Image domain approaches typically involve approximating the PSF, and iteratively solving for the inverse PSF, in accordance with Equation (5).

Sjoeberg et al. (2003) demonstrated that ray-based PSFs estimated via the approach illustrated in Figure 6, may be applied for successful deconvolution of Kirchhoff-modelled seismic data. Their approach involved rewriting Equation (6) in the normal-equation form followed by implementation of the conjugate-gradient method for iterative solving of the obtained equation. More specifically, Equation (6) represents the convolution between a localized PSF operator and the input reflectivity grid. Through lexicographical ordering of the PSF, this equation may be rewritten as a linear system of equations:

$$\bar{\mathbf{y}} = \mathbf{D}\bar{\mathbf{x}}, \quad (8)$$

where $\bar{\mathbf{y}}$ represents the blurred seismic image, $\bar{\mathbf{x}}$ is the original image (i.e., reflectivity model) and \mathbf{D} is the lexicographically ordered PSF. The normal-equation form of Equation (8) involves multiplying each side of the equation with the transpose of \mathbf{D} :

$$\mathbf{D}^T\bar{\mathbf{y}} = \mathbf{D}^T\mathbf{D}\bar{\mathbf{x}}. \quad (9)$$

Equation (9) may be solved through a variety of different iterative approaches. Frequently, a regularization term is also added to the equation:

$$\mathbf{D}^T\bar{\mathbf{y}} = (\mathbf{D}^T\mathbf{D} + \lambda\mathbf{I})\bar{\mathbf{x}}. \quad (10)$$

Here, λ is the chosen regularization parameter and \mathbf{I} is the identity matrix with same dimensions as $\mathbf{D}^T \mathbf{D}$. Regularization may be applied to dampen noise, but the trade-off is a reduction in resolution.

To illustrate the concept of PSF-based deconvolution, a target area of the 2D fault model extracted from a 3D-model presented in [Qu and Tveranger \(2016\)](#), and used by [Kolyukhin et al. \(2017\)](#) for statistical analyses of fault facies after seismic imaging of 2D FD-modelled data, is selected (Figure 18). Note that [Botter et al. \(2017\)](#) applied PSF-based convolution to model various PSDM results from the 3D model to test various seismic attributes. In this thesis, the same P-velocity values applied by [Botter et al. \(2017\)](#) are used.

The model itself is highly detailed, with a grid sampling of 1 meter in both x - and z -directions. An analytic PSF with a maximum dip range of 45° was selected. The average velocity used for the used for the PSF was set at 2.86 km/s based on velocity values at the target area. Though [Kolyukhin et al. \(2017\)](#) and [Botter et al. \(2017\)](#) used standard seismic frequencies in their modelling studies (10-60 Hz), a 100-Hz Ricker wavelet was used here for the sake of illustrating the results down to a finer pixel level. The input reflectivity model at the target area was then convolved with the PSF (Figure 19a) to yield a simulated PSDM image. Next, deconvolution was performed using the same PSF by implementing Equation (10) via the conjugate-gradient approach. As the PSF in this case was known in advance, no regularization was applied. The iterative tolerance error was set to 10^{-7} . Figure 19b illustrates the deconvolution procedure. Figure 19c and 19d further illustrate the convolution and deconvolution procedures within the smaller area highlighted by the yellow box in Figure 19a to better appreciate the results down to the 1-m pixel level.

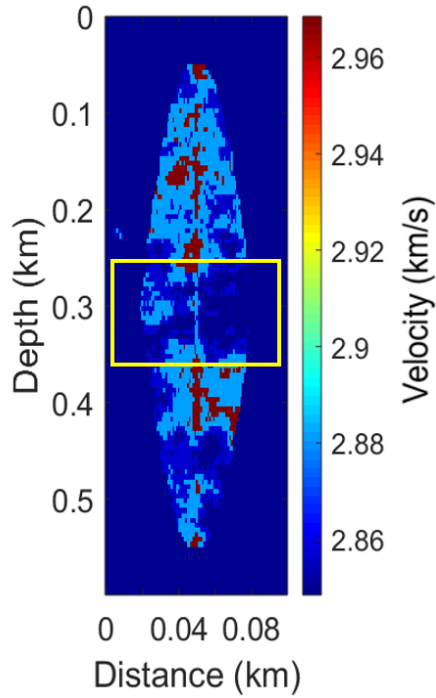


Figure 18: Fault velocity model with selected target area highlighted with the yellow box.

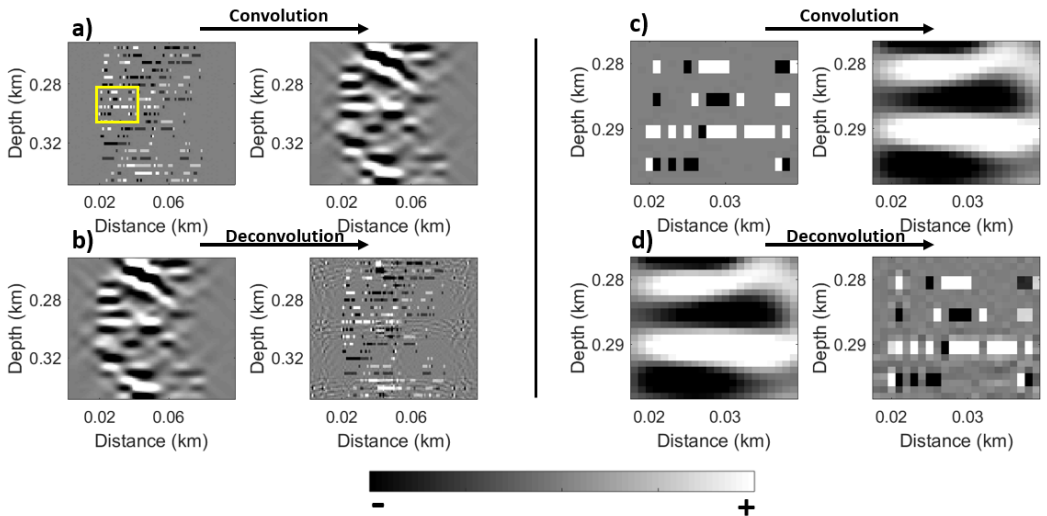


Figure 19 a): Convolution of input reflectivity grid and PSF. b) Deconvolution of simulated PSDM image. (c-d) Convolution and deconvolution at the zoomed-in area highlighted by the yellow box in a).

The reflectivity grid is well retrieved after deconvolution of the seismic images through implementation of Equation (10) (Figure 19b and 19d). Some noise is present in the deconvolved images, but it is most likely due to truncation effects at the edges of the reflectivity grid. Nevertheless, all geological features, even in such a complex model, are properly retrieved, which validates the deconvolution approach.

The retrieved reflectivity grid from deconvolution in Figure 19 stems, however, from the fact that the exact PSF used for the initial convolution was re-used for deconvolution, hence an ideal case. In practice, obtaining such exact PSFs is generally inherently difficult. As illustrated in previous sections, several features influence the ultimate illumination and resolution pattern of the PSF. Non-stationarity within target areas characterized by, e.g., high-velocity contrasts may furthermore require multiple PSFs to be estimated at various parts of the selected target area. To illustrate with a simple example how parameter errors in the PSF-operator may affect the deconvolved image, a PSF designed with the wrong velocity of 2 km/s was applied as a deconvolution operator on the obtained seismic image in Figure 19a. This error results in a seismic image plagued by more considerably more noise, as is shown Figure 20b.

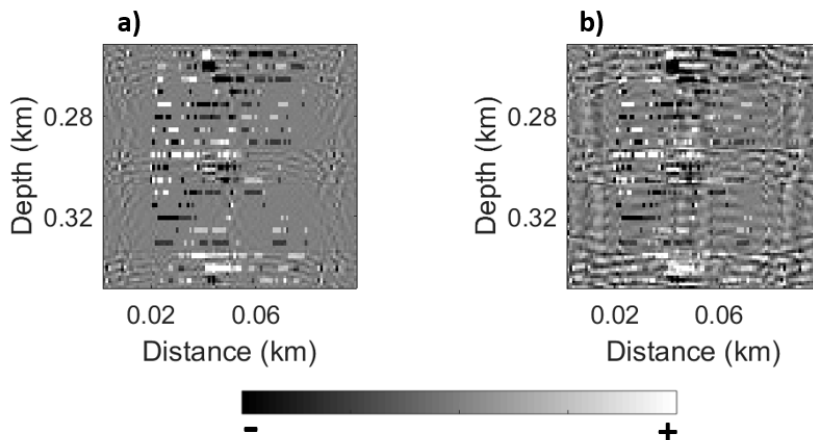


Figure 20: Deconvolution of simulated PSDM-image using PSF with a) correct velocity (2.86 km/s) and b) wrong velocity (2 km/s).

If the deconvolved image suffers from noise, a compromise might be to increase the regularization parameter to dampen noise issues caused by inaccuracies in the PSF and the presence of migration artefacts not captured in the PSF. The trade-off of that dampening, as pointed out, is a reduction in resolution. To illustrate this effect, we may consider the PSDM-image obtained after convolution in Figure 19a again, but this time with some random low-frequency (≤ 30 Hz), low-amplitude, noise (Figure 21) added to the image prior to deconvolution. Deconvolution was then performed using regularization parameters of 0, 0.05 and 0.5, respectively (Figure 22).

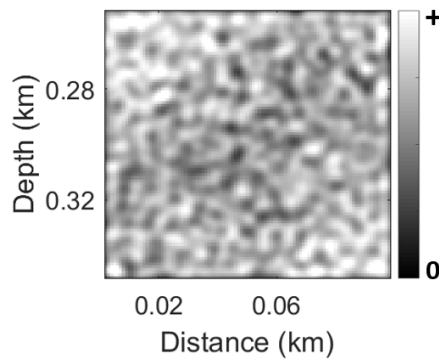


Figure 21: Random noise added to the simulated PSDM-image in Figure 19b prior to deconvolution.

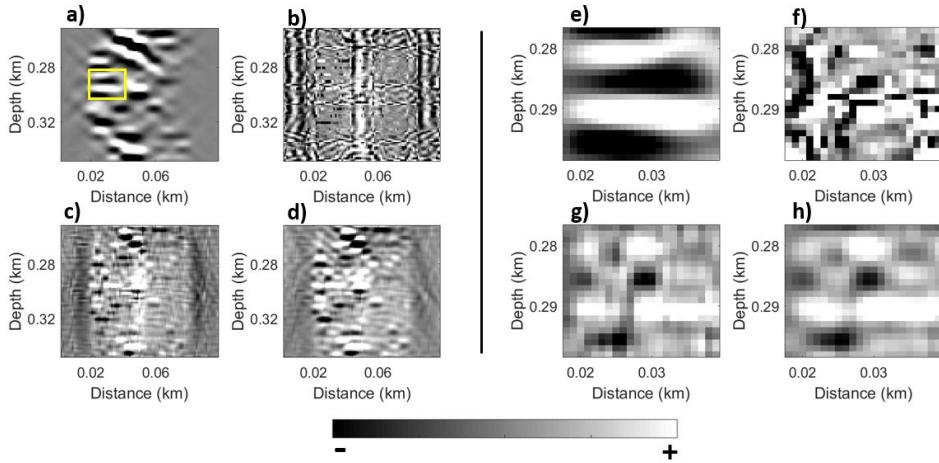


Figure 22: a) PSDM-image with added random noise prior to deconvolution. (b-d) Deconvolution with regularization parameter set to 0, 0.05 and 0.5, respectively. (e-h) PSDM-image and deconvolution results at the zoomed-in area highlighted by the yellow box in a).

A regularization parameter of 0 in this case results in a deconvolved image completely obscured by noise (Figure 22b and 22f). By increasing the regularization parameter, the noise is dampened, but resolution decreases with increasing regularization value, as expected (Figure 22c-22d and 22g-22h). Unlike the example illustrated in Figure 19, where the ideal PSF was applied, several geological details are not possible to retrieve in this case.

In summary, the case study illustrated here thus shows how ray-based PSFs may be applied as deconvolution operators in a completely controlled experiment. Due to the low computational cost required for the design of ray-based PSFs, adjustments of PSF-parameters may be done efficiently and with great flexibility when implemented on seismic data in general. Examples of how the method performs on seismic data obtained independently from PSF convolution are presented in the third paper included in this thesis.

1.8 Thesis contributions

The previous subsections outline the general principles behind PSFs, PSF convolution modelling, and PSF-based deconvolution. This subsection will now briefly summarize the novel contributions to the field which comprise the main bulk of this thesis. The contributions are presented in three separate research papers supplemented by two published SEG conference abstracts.

Paper 1 investigates in detail similarities and differences between PSFs obtained via wave-based and ray-based approaches. Analytical expressions valid in a homogeneous model are derived for wave-based and ray-based PSFs. The various parameters in the derived equations are analysed to assess the conditions in which divergence between the two approaches occurs. The analytically computed PSFs are also compared to PSFs obtained from full modelling and PSDM (reverse-time migration). Further assessments of simulated PSDM-images obtained via wave-based and ray-based PSFs are next performed at selected targets in a subsection of the BP Statics Benchmark model. The PSF-convolved images are also compared to the output from a full modelling followed by RTM. Comparisons are made as to how well the wave-based and ray-based approaches model illumination, resolution and amplitude effects observed in the migrated image. Similarities and differences between the wave- and ray-based PSF-convolved images are also analysed. A novel contribution to the field includes the full derivation of the governing equations for wave- and ray-based PSFs valid for the homogeneous case. In addition, very few comparative studies between fully modelled/migrated data and simulated seismic images obtained via ray-based and wave-based PSF convolution modelling exist. The paper thus also provides a novel contribution by providing such a comparative study.

Paper 1 was published in *Geophysical Prospecting* in July 2021.

Paper 2 investigates the potential for PSF convolution modelling as an efficient approach for seismic modelling of paleokarst geology. Although PSF convolution

modelling has been applied as a modelling tool on various other geological geobodies, the assessment of how well the method performs on highly complex paleokarst geology has not been done previously. The validity of the approach is first assessed through a comparison with results obtained from a physical modelling experiment conducted by [Xu et al. \(2016\)](#). Four separate case studies next highlight the usefulness and flexibility of the approach by focusing on different aspects related to PSF convolution modelling, as well as challenges inherent in characterizing and interpreting paleokarst features. The first case study involves a 2D model of the Franklin Mountains paleocaves where comparisons are made between simulated PSDM-images obtained after modelling with different wavelet peak frequencies. Comparisons are also made between a model where the cave system is embedded in a uniform background versus a model where background layers are included, so that assessments can be made as to how various petrophysical properties affect the PSDM-image. The second case study, a 3D geocellular model of the Stergrotta cave, focuses on how repeated-1D convolution and PSF convolution modelling may yield drastically different modelled images of complex paleokarst systems characterized by small-scale features. Case study three focuses on a 3D geocellular model of the Devil's Sinkhole. Comparisons are here made with previously modelled images of the sinkhole done by [Janson and Fomel \(2011\)](#) through an exploding-reflector split-step Fourier migration approach. As such, the validity of PSF convolution modelling is assessed by a direct comparison with results obtained from a different modelling algorithm. The Devil's Sinkhole case is further used to assess how limitations in illumination could greatly exacerbate sinkhole features in seismic data. Finally, the fourth study, which applies a 3D geocellular model of the Lechuguilia Cave, investigates how PSF convolution modelling may be used to assess how coarse sampling yields seismic images which do not properly account for lateral resolution effects. In summary, novel contributions to the field include the assessment of how PSF convolution modelling may be used as a seismic modelling approach specifically for paleokarst geology, as well as the assessment of how results obtained via this modelling approach compare to results obtained from other modelling approaches previously applied on the same geology.

Paper 2 was published in *Interpretation* (Vol. 9, Issue 2) May 2021.

Paper 3 focuses on the potential of applying ray-based PSFs as deconvolution operators on RTM images. As illustrated for the paleokarst case studies in Paper 2, seismic images usually exacerbate the true extent of geological features. Successful deconvolution of seismic images could therefore greatly enhance the level of detail and reduce this vertical and lateral exacerbation. To allow for deconvolution of seismic images through ray-based PSFs, the PSFs are defined in their normal-equation form, and a conjugate-gradient algorithm is implemented when solving for the unknown reflectivity grid. Deconvolution is performed on seismic images of point scatterers in a homogeneous model obtained from wave-equation based forward modelling followed by RTM. The deconvolved point scatterers are compared to results obtained via conventional source-signature deconvolution. Furthermore, for an assessment of the robustness of the approach, deconvolution is performed at a large target area of a fully modelled and reverse-time migrated image of the Sigsbee2A model. For this case study, multiple PSFs are applied at various grid locations within this target area, and each grid is deconvolved independently. The deconvolved grids are then finally combined into a complete deconvolved image of the entire target area. Novel contributions to the field thus include a thorough assessment of how well ray-based PSFs perform when used as deconvolution operators compared to conventional source-signature deconvolution, as well as an assessment of how ray-based PSFs may be applied as deconvolution operators on reverse-time migrated images. Due to the speed and flexibility with which ray-based PSFs may be designed, the approach holds great potential for reprocessing, for instance, legacy-seismic images, as well as being used as a quick technique for reducing the number of iterations required in, i.e., least-squares migration.

Paper 3 was submitted to *Geophysical Prospecting* in August 2021 and is currently in review.

Abstract 1 illustrates how ray-based PSF convolution modelling may be used to efficiently model how the altering of various migration parameters may affect illumination and resolution of seismic images. Specifically, the abstract focuses on how amplitude effects and choice of migration aperture width may influence seismic image quality. The effects of these parameters are assessed at two different target areas of the Sigsbee2A model. The novel contribution to the field is therefore the specific illustration of how ray-based PSFs may be used to assess how these two parameters affect PSDM-images.

Abstract 1 was presented as an oral presentation at SEG 2018 in Anaheim, CA, USA.

Abstract 2 presents preliminary work that ended up becoming **Paper 2**. The abstract presents a comparison of PSF-modelled seismic data and results obtained from the physical modelling experiment conducted by [Xu et al. \(2016\)](#). Preliminary results of The Devil's Sinkhole case study, described in greater detail under Paper 2, are also presented. Novel contributions are the same as for Paper 2 but limited only to the comparison with the physical modelling experiment and The Devil's Sinkhole case.

Abstract 2 was accepted as a poster presentation for SEG 2020 in Houston, TX, USA, but due to the coronavirus epidemic the presentation was given digitally over the Internet.

2. Conclusions and future perspectives

This study has evaluated the validity and potential of ray-based point-spread functions as seismic modelling and deconvolution operators. I will now summarize the main findings of each paper and provide some perspectives for potential future research directions.

Paper 1 illustrates how ray-based PSFs, when used as convolution operators, yield simulated PSDM-images comparable to equivalent images obtained from wave-based PSFs. Resolution-, illumination- and amplitude effects prevalent in PSDM-images are accurately captured, as verified by comparisons with actual PSDM-images obtained via RTM. Through the derivation of the governing equations valid for both wave-based and ray-based PSFs in a homogeneous medium, the conditions under which the two approaches may diverge are also assessed. The equations reveal that divergence occurs at targets characterized by short distance to shot point and high velocity. These conditions represent geologically unrealistic scenarios, thus indicating that ray-based PSFs may be applied as a valid supplement to more costly wave-based PSFs.

Having assessed in Paper 1 that PSF convolution modelling through ray-based PSFs indeed offers a valid alternative to more costly wave-based approaches, Paper 2 demonstrates how ray-based PSFs are suitable for modelling highly complex paleokarst geology. The validity of the approach is first assessed through a comparison with modelled results obtained from a published physical modelling experiment. Four separate case studies then illustrate how ray-based PSFs may be used to analyse how parameters such as survey design, petrophysical background properties, wavelet frequency, infill properties, illumination coverage and sampling all influence seismic paleokarst signatures. Due to the inherent small-scale heterogeneity of paleokarst features, it is demonstrated how the approach allows for accurate assessments of how the size and geometry of these features may be misrepresented in seismic data. Comparisons are also made with previously published synthetic seismic modelling results, thus further validating ray-based PSFs as an efficient supplemental alternative to other modelling approaches.

Finally, Paper 3 assesses how ray-based PSFs may also be applied as seismic deconvolution operators on reverse-time migrated images. By using the estimated PSFs as inputs in an iterative conjugate-gradient algorithm, resolution enhancement of migrated images may be rapidly obtained at a low computational cost. The approach is demonstrated on migrated point scatterers embedded in a homogeneous medium, and at a large target area of the Sigsbee2A velocity model. Comparisons are made with deconvolved results obtained via conventional source-signature deconvolution, and the examples demonstrate that PSF-based deconvolution provides better resolution improvement, particularly in the lateral direction. Thus, while Paper 1 and Paper 2 demonstrate and validate the potential of using ray-based PSFs as convolution operators for seismic modelling of PSDM-images, Paper 3 illustrates how ray-based PSFs may also be applied for inverse problems where the aim is to deblur seismic images.

Two abstracts included in the thesis offer some additional, supplemental results. The first abstract, presented at SEG 2018 in Anaheim, CA, USA, shows how ray-based PSFs may be fine-tuned for various sensitivity studies, with particular focus on how different choices of migration aperture width and amplitude mode may result in significantly different seismic images at target areas of interest. The second abstract, presented at the virtual SEG 2020 conference in Houston, TX, USA, presents preliminary work on seismic modelling of paleokarst, which ultimately ended up being included in Paper 2.

From the results presented in this thesis, there are several potential future research directions which may be considered. Although the findings from Paper 1 reveal that the simulated PSDM-images obtained through ray-based PSFs were virtually indistinguishable to images obtained through wave-based PSFs, more work should be done to assess whether this is the case for other complex models with different geological challenges. Furthermore, although the derived governing equations reveal that divergence should only be expected for geologically unrealistic scenarios, it is important to consider that the equations only account for a 2D homogeneous, isotropic medium. Further theoretical studies into how these equations may be modified for more

complex media are therefore desired. In general, as Paper 1 illustrates, migration artefacts, interference issues and wave-energy originating from outside the selected target area present in actual PSDM-images, may not be fully captured by simulated PSDM-images obtained from PSFs. A more thorough investigation of the mathematics involved in more complex cases, could reveal potential ways for PSFs to be designed in such a manner that these effects may be more accurately captured.

Several other research directions may also be considered for refinements of the PSF-operator. One option is to consider effects caused by anisotropy in the PSFs ([Lecomte and Kaschwich, 2008](#)). For large-scale 3D studies, such as the paleokarst case studies considered in Paper 2, it is reasonable to assume that anisotropic effects would occur in an actual seismic survey ([Feng et al., 2012](#); [Sun et al., 2012](#)). The PSF-operator could also be further refined by including a more precise description of how reflectivity is impacted by the range of incidence angles. Seismic resolution is determined by the combined effects of angle-dependent reflectivity and angle-dependent illumination/resolution ([Lecomte, 2008](#)), but only the latter has been considered in this thesis. Thus, most comparisons between modelled and migrated data had to rely on manual calibration and regularization of amplitude values. Further investigation into this topic could therefore be useful in providing a more accurate assessment of how modelled and migrated amplitudes vary.

The ray-based PSFs could be further refined by extending the plane-wave assumption, which has been a constant assumption in this thesis, to a parabolic assumption. This would allow for more accurate modelling of curvature effects present in migrated images and wave-based PSFs ([Gelius et al., 2002b](#)). Future studies could also assess whether ray-based PSFs may be used as realistic convolution operators for the simulation of elastic PSDM-images. The ray-based PSFs may be modified to model PS-converted waves by applying scaling factors to the individual wavenumber vectors in the wavenumber domain ([Gelius et al., 2002a](#)). As elastic wave-based PSFs are computationally expensive to obtain, accurately estimated ray-based PSFs for simulation of elastic images, could provide a fast alternative for modelling such images.

The abovementioned suggestions for future research could also yield ray-based PSFs capable of more accurate deconvolution. Although the findings of Paper 3 illustrate the potential of using ray-based PSFs in the deconvolution of reverse-time migrated images, it should be kept in mind that the results were obtained for synthetic models only. In addition, all acquisition- and processing parameters were known in advance. For actual seismic data obtained in the field, it is likely that many of the refinements suggested in this section may be required if proper deconvolution is desired. The lack of any real data used in this thesis is therefore something that should be acknowledged as a potential limitation of the findings. Future research should venture to more accurately assess how simulated PSDM-images obtained from PSF convolution modelling capture features observed in real data. Likewise, further assessments of how ray-based PSFs perform as deconvolution operators on real data are desired. This could yield more information as to which of the refinements outlined in this section may be most relevant to investigate further. It may also be worth assessing how iterative approaches other than the conjugate-gradient algorithm will perform when ray-based PSFs are used as deconvolution operators.

3. Bibliography

- Aoki, N. and Schuster, G.T. (2009). Fast least-squares migration with a deblurring filter. *Geophysics*, 74(6), pp. WCA83-WCA93.
- Arya, V.K. and Holden, H.D. (1978). Deconvolution of seismic data – an overview. *IEEE Transactions on Geoscience Electronics*, 16(2), pp. 95-98.
- Baysal, E., Kosloff, D. and Sherwood J. (1983). Reverse-time migration. *Geophysics*, 48, pp. 1514-1524.
- Beylkin, G., Oristaglio M., and Miller D. (1985). Spatial resolution of migration algorithms. In: A.J. Berkhout, J. Ridder and L.F. van der Waals, eds., *Proceedings of the 14th International Symposium on Acoustic Imaging*. Plenum Press., pp. 155-167.
- Botter, C., Cardozo, N., Hardy, S., Lecomte, I. and Escalona, A. (2014). From mechanical modeling to seismic imaging of faults: A synthetic workflow to study the impacts of faults on seismic. *Marine and Petroleum Geology*, 57, pp. 187-207.
- Botter, C., Cardozo, N., Qu, D., Tveranger, J. and Kolyukhin, D. (2017). Seismic characterization of fault facies models. *Interpretation*, 5(4), pp. SP9-SP26.
- Cao, C, J. (2013). Resolution/illumination analysis and imaging compensation in 3D dip-azimuth domain. In: *83rd SEG Annual International Meeting, Houston, TX, USA*, Expanded Abstracts, pp. 3931-3936.
- Carcione, J.M., Hermann, G.C. and ten Kroode, A.P.E. (2002). Seismic modeling. *Geophysics*, 67 (4), pp. 1304-1325.
- Červený, V., Molotkov, I.A. and Pšenčík, I. (1977). *Ray method in seismology*. Charles University, Prague.
- Claerbout, J.F. (1971). Toward a unified theory of reflector mapping. *Geophysics*, 36(3), pp. 467-481.
- Dai, W., Wang, X. and Schuster, G.T. (2011). Least-squares migration of multisource data with a deblurring filter. *Geophysics*, 76(5), pp. R135-R146.
- Dai, W., Fowler, P. and Schuster, G.T. (2012). Multi-source least-squares reverse time migration. *Geophysical Prospecting*, 60, pp. 681-695.
- Dai, W. and Schuster, G.T. (2013). Plane-wave least-squares reverse-time migration. *Geophysics*, 78(4), pp. S165-S177.

-
- Eide, C.H., Schofield, N., Lecomte, I., Buckley, S.J. and Howell, J.A. (2018). Seismic interpretation of sill complexes in sedimentary basins: Implications for the subsill imaging problem. *Journal of the Geological Society*, 175, pp. 193-209.
- Feng, X., Wang, Y., Wang, X., Wang, N., Gao, G., and Zhu, X. (2012). The application of high-resolution 3D seismic acquisition techniques for carbonate reservoir characterization in China. *The Leading Edge*, 31, pp. 168-179.
- Gelius, L.-J., Lecomte, I. and Tabti, H. (2002a). Analysis of the resolution function in seismic prestack depth imaging. *Geophysical Prospecting*, 50(5), pp. 505-515.
- Gelius, L.-J., Lecomte, I. and Hamran, S.-E. (2002b). The concept of local parabolic-wave imaging (LpI) in PSDM. In: *72nd SEG Annual International Meeting, Salt Lake City, UT, USA*, Expanded Abstracts, pp. P1184-1187.
- Gjøystdal, H., Iversen, E., Lecomte, I., Kaschwich, T., Drottning, Å. And Mispel, J. (2007). Improved applicability of ray tracing in seismic acquisition, imaging, and interpretation. *Geophysics*, 72(5), pp. SM261-SM271.
- Gray, S. (1997). True-amplitude seismic migration: A comparison of three approaches. *Geophysics*, 62(3), pp. 929-936.
- Grippa, A., Hurst, A., Palladino, G., Iacopini, D., Lecomte, I. and Huuse, M. (2019). Seismic imaging of complex geometry: Forward modeling of sandstone intrusions. *Earth and Planetary Science Letters*, 513, pp. 51-63.
- Guitton, A. (2004). Amplitude and kinematic corrections of migrated images for nonunitary imaging operators. *Geophysics*, 69, pp. 1017-1024.
- Hamran, S.-E. and Lecomte, I. (1993). Local plane-wavenumber diffraction tomography in heterogeneous backgrounds. Part 1: Theory. *Journal of Seismic Exploration*, 2, pp. 133-146.
- Hu, J., Schuster, G.T. and Valasek, P.A. (2001). Poststack migration deconvolution. *Geophysics*, 66, pp. 939-952.
- Jafarian, E., de Jong, K., Kleipool, L.M., Scheibner, C., Blomeier, D.P.G. and Reijmer, J.J.G. (2018). Synthetic seismic model of a Permian biosiliceous carbonate – carbonate depositional system (Spitsbergen, Svalbard Archipelago). *Marine and Petroleum Geology*, 92, pp. 78-93.
- Janson, X., and Fomel, S. (2011). 3-D forward seismic model of an outcrop-based geocellular model. In: O. Martinsen, A.J. Pulham, P.D. Haughton and M.D. Sullivan, eds., *Outcrops revitalized: tools, techniques and applications: SEPM Concepts in Sedimentology and Paleontology 10*. SEPM Society for Sedimentary Geology, pp. 87-106.

- Jensen, K., Lecomte, I. and Kaschwich, T. (2018). Analyzing PSDM images in complex geology via ray-based PSF convolution modeling. In: *88th SEG Annual International Meeting, Anaheim, CA, USA*, Expanded Abstracts, pp. P3843-3847.
- Jensen, K., Johansen, M.K., Lecomte, I., Janson, X., Tveranger, J. and Kaschwich, T. (2021a). Paleokarst reservoirs: Efficient and flexible characterization using point-spread-function-based convolution modeling. *Interpretation*, 9(2), pp. T331-T347.
- Jensen, K., Lecomte, I., Gelius, L.-J. and Kaschwich, T. (2021b). Point-spread function convolution to simulate prestack depth migrated images: A validation study. *Geophysical Prospecting*. (Accepted for publication).
- Jiang, B. and Zhang, J. (2019). Least-squares migration with a blockwise Hessian matrix: A prestack time-migration approach. *Geophysics*, 84(4), pp. R625-R640.
- Kaur, H., Pham, N., and Fomel, S. (2020). Improving the resolution of migrated images by approximating the inverse Hessian using deep learning. *Geophysics*, 85(4), pp. WA173-WA183.
- Kolyukhin, D.R., Lisitsa, V.V., Protasov, M.I., Qu, D., Reshetova, G.V., Tveranger, J., Tcheverda, V.A. and Vishnevsky, D.M. (2017). Seismic imaging and statistical analysis of fault facies models. *Interpretation*, 5(4), pp. SP71-SP82.
- Kühl, H. and Sacchi, M.D. (2003). Least-squares wave-equation migration for AVP/AVA inversion. *Geophysics*, 68, pp. 262-273.
- Lecomte, I. and Gelius, L.-J. (1998). Have a look at the resolution of prestack depth migration for any model, survey and wavefields. In: *68th SEG Annual International Meeting, New Orleans, LA, USA*, Expanded Abstracts, pp. P1112-1115.
- Lecomte, I., Gjøystdal, H. and Drottning, Å. (2003). Simulated prestack local imaging: a robust and efficient interpretation tool to control illumination, resolution, and time-lapse properties of reservoirs. In: *73rd SEG Annual International Meeting, Dallas, TX, USA*, Expanded Abstracts, pp. P1525-1528.
- Lecomte, I. (2008). Resolution and illumination analyses in PSDM: A ray-based approach. *The Leading Edge*, 27, pp. 650-663.
- Lecomte, I. and Kaschwich, T. (2008). Closer to real earth in reservoir characterization: A 3D isotropic/anisotropic PSDM simulator. In: *78th SEG Annual International Meeting, Las Vegas, NV, USA*, Expanded Abstracts, pp. P1570-1574.

-
- Lecomte, I., Lavadera, P.L., Anell, I., Buckley, S.J., Schmid, D.W. and Heeremans, M. (2015). Ray-based seismic modeling of geological models: Understanding and analyzing seismic images efficiently. *Interpretation*, 3(4), pp. SAC71-SAC89.
- Lecomte, I., Lubrano-Lavadera, P., Botter, C., Anell, I., Buckley, S.J., Eide, C.H., Grippa, A., Mascolo, V. and Kjoberg, S. (2016). 2(3)D convolution modelling of complex geological targets – beyond 1D convolution. *First Break*, 34, pp.99-107.
- Nemeth, T., Wu, C., and Schuster, G.T. (1991). Least-squares migration of incomplete reflection data. *Geophysics*, 64, pp. 208-221.
- Paffenholz, J., Stefani, J., McLain, B. and Bishop, K. (2002). SIGSBEE_2A synthetic subsalt dataset – image quality as function of migration algorithm and velocity model error. In: *64th EAGE Conference & Technical Exhibition, Florence, Italy*, Expanded Abstracts, pp. B019.
- Podvin, P. and Lecomte, I. (1991). Finite-difference computation of traveltimes in very contrasted velocity models: a massively parallel approach and its associated tools. *Geophysical Journal International*, 105(1), pp. 271-284.
- Qu, D. and Tveranger, J. (2016). Incorporation of deformation band fault damage zones in reservoir models. *AAPG Bulletin*, 100, pp. 423-443.
- Rabbell, O., Galland, O., Mair, K., Lecomte, I., Senger, K., Spacapan, J.B. and Manceda, R. (2018). From field analogues to realistic seismic modelling: A case study of an oil-producing andesitic sill complex in the Neuquén Basin, Argentina. *Journal of the Geological Society*, 175, pp. 580-593.
- Rickett, J.E. (2003). Illumination-based normalization for wave-equation depth migration. *Geophysics*, 68, pp. 1371-1379.
- Robinson, E.A., and Treitel, S. (1978). The fine structure of the normal incidence synthetic seismogram. *Geophysical Journal of the Royal Astronomical Society*, 53, pp. 289-309.
- Schuster, G.T. and Hu, J. (2000). Green's function for migration: Continuous recording geometry. *Geophysics*, 65(1), pp. 167-175.
- Schuster, G.T. (2017). *Seismic Inversion*. Society of Exploration Geophysicists.
- Sjoeborg, T.A., Gelius, L.-J. and Lecomte, I. (2003). 2-D deconvolution of seismic image blur. In: *73rd SEG Annual International Meeting, Dallas, TX, USA*, Expanded Abstracts, pp. 1055-1059.

- Sun, S.Z., Chen, L., Xiao, X., Liu, L., Tang, Z., Wei, J. and Sun, L. (2012). Studying heterogeneity and anisotropy via numerical and physical modeling. *The Leading Edge*, 31, pp. 190-196.
- Tang, Y. (2009). Target-oriented wave-equation least-squares migration/inversion with phase-encoded Hessian. *Geophysics*, 74(6), pp. WCA95-WCA107.
- Tarantola, A. (1984). Inversion of seismic reflection data in the acoustic approximation. *Geophysics*, 49, pp. 1259-1266.
- Toxopeus, G., Petersen, S. and Wapenaar, K. (2003). Improving geological modeling and interpretation by simulated migrated seismics. In: *65th EAGE Annual Conference and Exhibition, Stavanger, Norway*, Expanded Abstracts, pp. F34.
- Toxopeus, G., Thorbecke, J., Wapenaar, K., Petersen, S., Slob, E. and Fokkema, J. (2008). Simulating migrated and inverted seismic data by filtering a geologic model. *Geophysics*, 73(2), pp. T1-T10.
- Valenciano, A.A., Biondi, B. and Guitton, A. (2006). Target-oriented wave-equation inversion. *Geophysics*, 70(4), pp. A35-A38.
- Vinje, V., Iversen, E. and Gjøystdal, H. (1993). Traveltime and amplitude estimation using wavefront construction. *Geophysics*, 58 (8), pp. 1157-1166.
- Wang, N., Xie, X.-B., Duan, M., Li, D. and Wu, R.-S. (2019). Improving seismic image resolution in a carbonate fracture region: A case study. In: *89th SEG Annual International Meeting, San Antonio, TX, USA*, Expanded Abstracts, pp. 32-36.
- Wrona, T., Fossen, H., Lecomte, I., Eide, C.H. and Gawthorpe, R.L. (2020). Seismic expression of shear zones: Insights from 2-D point-spread-function based convolution modelling. *Journal of Structural Geology*, 140, 104121.
- Xie, X.-B., Wu, R.-S., Fehler, M. and Huang, L. (2005). Seismic resolution and illumination: A wave-equation based analysis. In: *75th SEG Annual International Meeting, Houston, TX, USA*, Expanded Abstracts, pp. P1862-1865.
- Xu, C., Di, B. and Wei, J. (2016). A physical modeling study of seismic features of karst cave reservoirs in the Tarim Basin, China. *Geophysics*, 81(1), pp. B31-B41.
- Xu, P., Wang, H., Guo, S. and Wu, C. (2020). RTM deblurring with flexible WKBJ PSFs. In: *90th SEG Annual International Meeting, Houston, TX, USA*, Expanded Abstracts, pp. 3083-3087.

- Xue, Z., Chen, Y., Fomel, S. and Sun, J. (2016). Seismic imaging of incomplete data and simultaneous-source data using least-squares reverse time migration with shaping regularization. *Geophysics*, 81(1), pp. S11-S20.
- Youzwishen, C.F. and Margrave, G.F. (1999). *Finite-difference modelling of acoustic waves in Matlab*. Crewes Report 11, pp. 1-19.
- Yu, J.J., Hu, G., Schuster, G.T. and Estill, R. (2006). Prestack migration deconvolution. *Geophysics*, 71(2), pp. S53-S62.
- Zhao, Z. and Sen, M. (2018). Fast image-domain target-oriented least-squares reverse time migration. *Geophysics*, 83(6), pp. A81-A86.

4. Papers

The following section includes the three papers which present the main scientific contributions in this thesis. As the first two papers are published, they will be presented in their respective journal formats. The page numbering thus deviates from the thesis page numbers for these two papers. The third paper, which is currently in review, will be presented in the submitted Microsoft Word-format. Following the three main papers, two accepted SEG-abstracts are presented. These are presented in their published format.

4.1 Paper 1

Point-spread function convolution to simulate prestack depth migrated images: A validation study

Kristian Jensen^{1*}, Isabelle Lecomte¹, Leiv Jacob Gelius² and Tina Kaschwich³

¹Department of Earth Science, University of Bergen, PO Box 7803, Bergen, 5020, Norway, ²Department of Geosciences, University of Oslo, PO Box 1047, Oslo, 0316, Norway, and ³NORSAR, Gunnar Randers vei 15, Kjeller, N-2007, Norway

Received November 2020, revision accepted June 2021

ABSTRACT

Seismic migration commonly yields an incomplete reconstruction of the Earth model due to restricted survey aperture, band-limited frequency content and propagation effects. This affects both illumination and resolution of the structures of interest. Through the application of spatial convolution operators commonly referred to as point-spread functions, simulated prestack depth-migrated images incorporating these effects may be obtained. Such simulated images are tailored for analysing distortion effects and enhance our understanding of seismic imaging and subsequent interpretation. Target-oriented point-spread functions may be obtained through a variety of waveform and ray-based approaches. Waveform approaches are generally more robust, but the computational cost involved may be prohibitive. Ray-based approaches, on the other hand, allow for efficient and flexible sensitivity studies at a low computational cost, but inherent limitations may lead to less accuracy. To yield more insight into the similarities and differences between point-spread functions obtained via these two approaches, we first derive analytical expressions of both wave- and ray-based point-spread functions in homogeneous media. By considering single-point scatterers embedded in a uniform velocity field, we demonstrate the conditions under which the derived equations diverge. The accuracy of wave-based and ray-based point-spread functions is further assessed and validated at selected targets in a subsection of the complex BP Statics Benchmark model. We also compare our simulated prestack depth migrated images with the output obtained from an actual prestack depth migration (reverse time migration). Our results reveal that both the wave- and ray-based approaches accurately model illumination, resolution and amplitude effects observed in the reverse time-migrated image. Furthermore, although some minor deviations between the wave-based and ray-based approaches are observed, the overall results indicate that both approaches can be used also for complex models.

Key words: Imaging, Modelling, Rays, Seismics, Wave.

INTRODUCTION

Migration of seismic data aims to backpropagate the scattered elastic energy to reconstruct the subsurface structure (e.g. reflectors and point scatterers). However, due to a re-

stricted survey aperture, band-limited frequencies and propagation effects in the overburden, migrated images inevitably yield a blurred and incomplete reconstruction of the actual Earth structures. In some cases, interference issues resulting from poor resolution may be so severe that important geological features become very difficult to identify, even when they are illuminated. As such, vital subsurface information may be

*E-mail: kristian.jensen@uib.no

lost. An understanding of how these blurring and illumination effects occur during seismic imaging is important for proper interpretation of migrated seismic images.

For a given reflectivity model, \mathbf{m} , we may compute synthetic seismic traces, \mathbf{d} , via the equation $\mathbf{d} = \mathbf{L}\mathbf{m}$, where \mathbf{L} is an applied forward modelling operator. A migrated image may then be obtained from the equation $\mathbf{m}_{\text{mig}} = \mathbf{L}^T \mathbf{L}\mathbf{m}$ (Schuster and Hu, 2000), with \mathbf{L}^T representing an approximation of the inverse \mathbf{L} -operator. The blurring effects observed in migrated seismic data are now mathematically expressed through the $\mathbf{L}^T \mathbf{L}$ -operator, commonly referred to as the local point-spread functions (PSFs). Information about the local illumination, as well as the overall resolution, may be retrieved by analysing the PSFs, i.e. the point-scatterer response of the seismic imaging system (Beylkin *et al.*, 1985; Lecomte and Gelius, 1998; Gelius *et al.*, 2002a). This type of information can, in turn, be analysed for assessing how the choice of, e.g., survey geometry, source wavelet, migration aperture, imaging condition, amplitude corrections and other processing parameters affects the seismic image. When PSFs are used as 2(3)D convolution operators applied to an incident angle-dependent input reflectivity grid, simulated prestack depth-migrated (PSDM) images incorporating these resolution and illumination effects are obtained (Lecomte *et al.*, 2003; Toxopeus *et al.*, 2003; Lecomte, 2008; Toxopeus *et al.*, 2008). Thus, realistic seismic images can be easily and rapidly simulated based on possibly complex geomodels (Lecomte *et al.*, 2003).

In addition to allowing for simulation of migration effects, accurate target-oriented PSFs may be used for other applications as well. Several studies demonstrate how the local PSF, or an estimate of its inverse, can be used for target-oriented migration and inversion (e.g. Schuster and Hu, 2000; Sjoeborg *et al.*, 2003; Guitton, 2004; Xie *et al.*, 2005; Valenciano *et al.*, 2006; Yu *et al.*, 2006; Aoki and Schuster, 2009; Tang, 2009; Ayeni and Biondi, 2010; Zhao and Sen, 2018; Jiang and Zhang, 2019). Fehler *et al.* (2005) propose to use PSFs to analyse how the choice of the migration operator affects image resolution. Thomson *et al.* (2016) demonstrate how the blurring function may be expressed as extended image gathers. This approach may be used to assess how blurring varies with the incidence slowness vector and reflectivity angle. Lecerf and Besselièvre (2018) show how PSFs may be successfully applied in 4D time-lapse reservoir monitoring. Fast and efficient methods for the estimation of accurate target-oriented PSFs are therefore of ongoing interest.

Target-oriented PSFs are frequently estimated by various wave-equation-based approaches. Xie *et al.* (2005) illustrate how target-oriented PSFs may be obtained using a one-

way wave-equation-based propagator to downward extrapolate the source functions and the receiver wavefields. Toxopeus *et al.* (2008) estimate PSFs by applying a one-way wave equation as previously outlined in Thorbecke *et al.* (2004). They demonstrate how these PSFs may be useful for both simulating defocusing in migration images and as inputs for inversion algorithms. Tang (2009) illustrates how PSFs may be retrieved using a one-way wave-equation-based Fourier finite-difference migration (Ristow and Rühl, 1994) and then used to approximate the inverse Hessian operator for target-oriented inversion.

As an alternative to wave-equation-based approaches, Gelius *et al.* (1991), Hamran and Lecomte (1993) and Lecomte and Gelius (1998) describe how target-oriented PSFs may be estimated at a much lower computational cost with the use of ray theory. Both ray-based and wave-equation-based approaches for estimating PSFs have their advantages and drawbacks. As for seismic modelling in general (see e.g. Carcione *et al.* 2002 for an in-depth review of advantages and disadvantages of various seismic modelling approaches), the choice of method is often made as a trade-off between accuracy and computing cost, although, in some cases of highly complex geology, ray-based approaches may not work properly. Ray-based methods generally suffer from drawbacks inherent in the high-frequency approximation used in ray tracing, such as incomplete wavefield, the requirement of a smooth velocity field, multipathing, the risk of breakdown in singular, caustic regions, etc. (Červený *et al.*, 1977). However, ray approaches are often more robust than assumed (Gjøystdal *et al.*, 2007), especially when applied to the rather smooth velocity models used for migration. Their low computational cost allows for fast and flexible modelling of how various migration parameters cause blurring and illumination effects in PSDM images (Lecomte *et al.*, 2016; Jensen *et al.*, 2018).

Although ray-based PSF convolution modelling has been applied in several geological case studies (e.g. Botter *et al.*, 2014; Lecomte *et al.*, 2015; Botter *et al.*, 2017; Kjøberg *et al.*, 2017; Eide *et al.*, 2018; Rabbel *et al.*, 2018; Grippa *et al.*, 2019; Lubrano-Lavadera *et al.*, 2019; Jensen *et al.*, 2021), comparative studies between waveform-based modelled/migrated data and simulated seismic images obtained via ray-based and wave-based PSF convolution modelling are limited. Lecomte *et al.* (2003) illustrate how PSF-convolved images obtained from ray tracing match well with Kirchhoff PSDM images obtained from a model of the Gullfaks field located on the Norwegian Continental Shelf. Toxopeus *et al.* (2008) compare results obtained via wave-equation-generated PSFs with actual time-migrated seismic images of

sulphate dissolution and karst collapse-related deformation. The authors demonstrate an improvement in the modelled results compared with results obtained via repeated 1D convolution. Amini *et al.* (2020) compare prestack Kirchhoff time-migrated results with modelled results obtained after applying a lateral smoothing function aiming at reproducing lateral smoothing effects (Chen and Schuster, 1999), to repeated 1D convolved results. This approach, as illustrated by the authors, yields more similar migrated and modelled images. Yet, a more thorough analysis of how PSF-convolved images obtained via different approaches compare to actual PSDM images is needed. This applies particularly for ray-based approaches where few comparative studies exist.

In the present work, we start by deriving analytical expressions for wave-based and ray-based PSFs valid for homogeneous media. By considering the case of single-point scatterers embedded in a uniform background, analytical modelling based on either wave- or ray-based implementations can be compared with output from an actual PSDM. Possible limitations inherent in the ray-based approach are identified and discussed. We then employ a subsection of the complex BP Statics Benchmark model (Ellison and Innanen, 2016) and assess how wave-based and ray-based PSF-convolved seismic images at selected targets compare to the output from a full PSDM of the subsection obtained via reverse time migration (RTM). Similarities and differences between the results obtained from the two modelling approaches are also assessed and discussed. The results may add to our understanding of the potential applications, as well as possible limitations, of using wave-based and ray-based PSF convolution as an approach for simulating PSDM images.

THE POINT-SPREAD FUNCTION IN A HOMOGENEOUS MEDIUM

A migrated image, \mathbf{m}_{mig} , is related to a model quantity, \mathbf{m} , via the equation:

$$\mathbf{m}_{\text{mig}} = \mathbf{L}^{-1} \mathbf{L} \mathbf{m}, \quad (1)$$

where \mathbf{L} is a forward modelling operator, and \mathbf{L}^{-1} is a stable approximation of its inverse. Assuming the Born approximation holds, the modelling operator, \mathbf{L} , may, for a single angular frequency value, be defined as

$$\mathbf{L} \rightarrow \omega^2 \int S(\omega) G(\omega, \mathbf{r}'|\mathbf{r}_s) G(\omega, \mathbf{r}_g, \mathbf{r}') d\mathbf{r}', \quad (2)$$

where ω is angular frequency, $S(\omega)$ is the wavelet spectrum, $G(\omega, \mathbf{r}'|\mathbf{r}_s)$ represents the Green's function from the source at

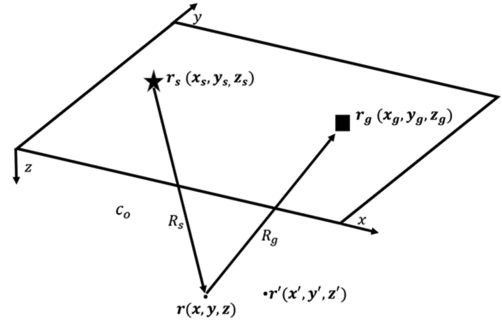


Figure 1 Survey geometry and relevant parameters for a single shot-receiver pair in a homogeneous model

\mathbf{r}_s to the image point at \mathbf{r}' , and $G(\omega, \mathbf{r}_g|\mathbf{r}')$ the Green's function from the image point at \mathbf{r}' to the receiver at \mathbf{r}_g . The Green's functions are, following the Born approximation, computed in the background media. A complete derivation of the Born approximation may be found in e.g. Bleistein *et al.* (2001) and Schuster (2017).

We now consider a homogeneous medium with an image point of interest at \mathbf{r} and a neighbouring point at \mathbf{r}' . Further, we assume a source located at position \mathbf{r}_s , and a receiver at position \mathbf{r}_g . The medium has a constant background velocity of c_0 . We denote the distance from \mathbf{r}_s to \mathbf{r} as $R_s(\mathbf{r}) = |\mathbf{r} - \mathbf{r}_s|$, and the distance from \mathbf{r}_g to \mathbf{r} as $R_g(\mathbf{r}) = |\mathbf{r} - \mathbf{r}_g|$. Figure 1 illustrates the survey geometry and the involved parameters.

Using these initial assumptions, and the survey geometry in Figure 1, we may now derive analytical expressions for the PSF generated at the point of interest in the homogeneous medium.

Wave-equation approach

Within a wave-equation approach, the inverse operator \mathbf{L}^{-1} is usually approximated through the adjoint operator, \mathbf{L}^T . The PSF is then expressed via the operator $\mathbf{L}^T \mathbf{L}$, which accounts for how limited illumination, overburden propagation and frequency bandwidth blur the migrated image. The migration equation may now, in the model space, be expressed as

$$\mathbf{m}(\mathbf{r})_{\text{mig}} = \int_{\text{model space}} \text{PSF}_{\text{wave}}(\mathbf{r}|\mathbf{r}') \mathbf{m}(\mathbf{r}') d\mathbf{r}'. \quad (3)$$

Here $\mathbf{m}(\mathbf{r}')$ represents the perturbed slowness at the point \mathbf{r}' :

$$\mathbf{m}(\mathbf{r}') \cong \frac{2}{c_0(\mathbf{r}')} \left[\frac{1}{c(\mathbf{r}')} - \frac{1}{c_0(\mathbf{r}')} \right], \quad (4)$$

with c_0 representing the reference, or background, velocity, and c representing the actual medium velocity at \mathbf{r}' . $\text{PSF}_{\text{wave}}(\mathbf{r}|\mathbf{r}')$ is the PSF which, for a *single shot* and using the definition for L in (2), is defined as (Schuster, 2017, p. 211)

$$\text{PSF}_{\text{wave}}(\mathbf{r}|\mathbf{r}') = \int_{\omega} \int_{\mathbf{r}_g} \omega^4 |S(\omega)|^2 G(\omega, \mathbf{r}_g|\mathbf{r})^* G(\omega, \mathbf{r}|\mathbf{r}_s)^* G(\omega, \mathbf{r}_g|\mathbf{r}') G(\omega, \mathbf{r}'|\mathbf{r}_s) d\mathbf{r}_g d\omega. \quad (5)$$

Here, a star represents the complex conjugate operation, and this equation can be interpreted as the migration response at point \mathbf{r} due to a point scatterer at \mathbf{r}' . The multiplication of the downgoing source field with the back-propagated reflections in (5) represents a standard cross-correlation imaging condition (Claerbout, 1971).

For a homogeneous 3D medium, we may define the far-field Green's functions analytically by

$$G = \frac{\exp(-ikR)}{4\pi R}, \quad (6)$$

where k is the wavenumber and R is the distance between two points of interest. Inserted into (5), and using the parameter definitions from Figure 1, as well as the relation $k = \omega/c_0$, we obtain the analytical expression for the PSF for a single shot and a point scatterer in a homogeneous 3D medium:

$$\text{PSF}_{\text{wave,3D}}(\mathbf{r}, \mathbf{r}') = \int_{\omega} \int_{x_g} \frac{\omega^4 |S(\omega)|^2}{256\pi^4 R_g(\mathbf{r}) R_g(\mathbf{r}') R_s(\mathbf{r}) R_s(\mathbf{r}')} \times \exp\left[\frac{i\omega}{c_0} (R_s(\mathbf{r}) + R_g(\mathbf{r}) - R_s(\mathbf{r}') - R_g(\mathbf{r}'))\right] d\mathbf{r}_g d\omega. \quad (7)$$

For a homogeneous 2D medium, the Green's function is defined analytically by

$$G = -\frac{i}{4} H_0^1(kR), \quad (8)$$

where k and R represent the same parameters as in (6), and $H_0^1(kR)$ is the zeroth order Hankel function of the first kind. Assuming a far-field approximation (for $kR \gg 1$), this function is approximated as

$$H_0^1(kR) \approx \sqrt{\frac{2}{\pi kR}} \exp\left[i\left(kR - \frac{\pi}{4}\right)\right]. \quad (9)$$

Through (8) and (9), we then obtain the analytical expression for the PSF for a single shot and a point scatterer in a homogeneous 2D medium:

$$\text{PSF}_{\text{wave,2D}}(\mathbf{r}, \mathbf{r}') = \int_{\omega} \int_{x_g} \frac{c_0^2 \omega^2 |S(\omega)|^2}{64\pi^2 \sqrt{R_g(\mathbf{r}) R_g(\mathbf{r}') R_s(\mathbf{r}) R_s(\mathbf{r}')}} \times \exp\left[\frac{i\omega}{c_0} (R_s(\mathbf{r}) + R_g(\mathbf{r}) - R_s(\mathbf{r}') - R_g(\mathbf{r}'))\right] dx_g d\omega. \quad (10)$$

We now proceed to derive the corresponding ray-based approach.

Ray-based approach

In our ray-based approach, we take inspiration from the local imaging method derived from local plane-wavenumber diffraction tomography (Hamran and Lecomte, 1993). We consider a small volume V_0 around the image point of interest. We assume that the Born approximation holds in this region, and that the background slowness is locally homogeneous. Moreover, we assume that the incident and scattered wavefields are plane within the volume (Hamran and Lecomte, 1993; Gelius *et al.*, 2002a). We let \mathbf{r} denote the location of an image point of interest, and \mathbf{r}' a reference point within the same volume.

Using a ray-based approach, we may define the Green's functions via the high-frequency approximation:

$$G(\omega, \mathbf{r}_j|\mathbf{r}) = A(\omega, \mathbf{r}_j|\mathbf{r}) \exp[i\omega\tau(\mathbf{r}_j|\mathbf{r})], \quad j = s, g, \quad (11)$$

where $A(\omega, \mathbf{r}_j|\mathbf{r})$ represents the complex amplitude, and τ is the travelt ime between a source (or receiver) and the image point. Assuming constant amplitude and a linear phase within the local volume V_0 , we can Taylor expand the Green's function around the reference point, \mathbf{r}' :

$$G(\omega, \mathbf{r}_j|\mathbf{r}) \cong G(\omega, \mathbf{r}_j|\mathbf{r}') \exp[i\omega\nabla\tau(\mathbf{r}_j|\mathbf{r}')(\mathbf{r} - \mathbf{r}')]. \quad (12)$$

We now introduce the scattering wavenumber vector \mathbf{K} defined by

$$\mathbf{K} = -\omega [\nabla\tau_s(\mathbf{r}|\mathbf{r}_s) + \nabla\tau_g(\mathbf{r}_g|\mathbf{r})] = -\mathbf{k}_s + \mathbf{k}_g, \quad (13)$$

where τ_s is the travelt ime from source point to \mathbf{r} , and τ_g is the travelt ime from \mathbf{r} to receiver point. It can be shown that \mathbf{K} represents the Fourier vector of the model space (Gelius, 1995), meaning the Fourier transform of the model space coordinates. This means that for each shot–receiver combination over the model space, a scattering wavenumber vector can be defined in the wavenumber domain. The entire collection of scattering wavenumber vectors will then yield the local wavenumber domain representation of the PSF. Thus, the expression in (13) links the model and acquisition domains.

We assume now that the phase of the wavefield varies significantly faster than the amplitude changes within the local volume of interest. At the same time, unlike in (10), we ensure that the PSF is normalized with respect to the reflectivity. The following ray-based approximation of the inverse of the

modelling operator L may then be derived (Gelius *et al.*, 1991; Gelius, 1995):

$$L^{-1} = \frac{J[\mathbf{K}|\omega, \mathbf{r}_g]}{\omega^4 |S(\omega)| |A_s|^2 |A_g|^2} L^T. \quad (14)$$

Here, $J[\mathbf{K}|\omega, \mathbf{r}_g]$ represents a Jacobian, derived in full in the Appendix, that maps between the Fourier-transformed model (scattering wavenumber) domain and the acquisition domain illustrated in Figure 1. In the general case, all quantities needed to compute it can be obtained from dynamic ray tracing. The inverse operator expressed in (14) is obtained from the use of a deconvolution imaging condition (Claerbout, 1971). Through (11)–(14) and the definition of the forward modelling operator L from (2), we obtain an expression for the ray-based PSF, under a Born-scattering assumption, valid for both 3D and 2D media (Gelius *et al.*, 2002a):

$$\text{PSF}_{\text{ray}}(\mathbf{r}|\mathbf{r}') = \int_{\mathbf{K}} |S(\omega)| \exp[i\mathbf{K} \cdot (\mathbf{r} - \mathbf{r}')] d\mathbf{K}, \quad (15)$$

where $d\mathbf{K} = J[\mathbf{K}|\omega, \mathbf{r}_g] d\omega d\mathbf{r}_g$. Here, the PSF is represented as a sum over all the scattering wavenumber vectors at the image point of interest, and the source spectrum $|S(\omega)|$ is included as an obliquity factor for the Born case. The equation represents an inverse Fourier transform, yielding a real-valued PSF in the spatial domain.

To allow for direct comparisons between wave-generated and ray-generated PSFs, we consider the analytical expression for the ray-based PSFs valid for a single shot and a point scatterer in a homogeneous 2D medium. By inserting the parameters defined in Figure 1 into Equation (15), the following analytical solution, derived in full in the Appendix, is obtained:

$$\begin{aligned} \text{PSF}_{\text{ray},2D}(\mathbf{r}, \mathbf{r}') &= \int_{\omega} \int_{x_g} \frac{\omega^2 |S(\omega)| \left[\alpha |(z - z_g)(x - x_g)| + \beta (z - z_g)^2 \right]}{c_0^2 R_s(\mathbf{r}) R_g(\mathbf{r})^4} \\ &\quad \times \exp \left[\frac{i\omega}{c_0} (R_s(\mathbf{r}) + R_g(\mathbf{r}) - R_s(\mathbf{r}') - R_g(\mathbf{r}')) \right] dx_g d\omega, \end{aligned} \quad (16)$$

where

$$\alpha = |(x - x_s) R_g(\mathbf{r}) - (x_g - x) R_s(\mathbf{r})|,$$

and

$$\beta = |(z - z_s) R_g(\mathbf{r}) - (z_g - z) R_s(\mathbf{r})|.$$

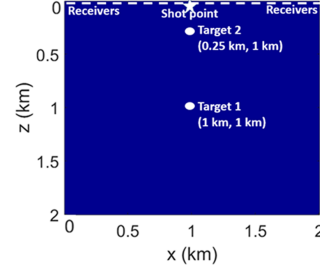


Figure 2 Homogeneous 2D model. Size: 2 km \times 2 km. Sampling interval: $dx = dz = 0.01$ km. Source location: $(x, z) = (1 \text{ km}, 0.01 \text{ km})$. Fixed receiver array consists of 200 equally spaced receivers (0.01 km interval) at depth $z = 0.01$ km.

Validation in the homogeneous case

To validate the derived equations, we consider two targets (targets 1 and 2) in the homogeneous 2D model illustrated in Figure 2. Two versions of the model were used, one with a constant velocity of 2 km/s (low-velocity model) and one with a constant velocity of 4 km/s (high-velocity model). We use two versions to demonstrate how the background velocity affects the PSF estimation.

Using a 2D acoustic finite-difference (FD) approach on a regular grid, we performed forward modelling for a single shot and a fixed receiver array located along the top row (Fig. 2). To implement the FD code, the domain was discretized with a second- to fourth-order scheme (second-order in time and fourth-order in space) following the numerical implementation presented in Youzwishen and Margrave (1999). A standard zero-phase Ricker wavelet with a peak frequency of 10 Hz was used as a source pulse, and the temporal sample interval was 1 ms. Although a combination of high velocity and low-frequency wavelet is geologically unrealistic for shallow targets, which we get for target 2 in the $v = 4$ km/s case, we deliberately chose these parameters to illustrate where the divergence between the wave-based and ray-based approaches occurs from a theoretical point. Half-spaces were added to all edges of the models to avoid reflections from the edges. Finally, a reverse time migration (RTM) was performed on the seismograms to obtain the responses from the point scatterers.

The obtained PSFs were extracted at both targets from the migrated images using a window of size 0.4 km times 0.4 km (41 \times 41 grid points), with the PSF centred at the middle of the window. Correspondingly, PSFs for both targets were calculated from Equations (10) and (16) using the same

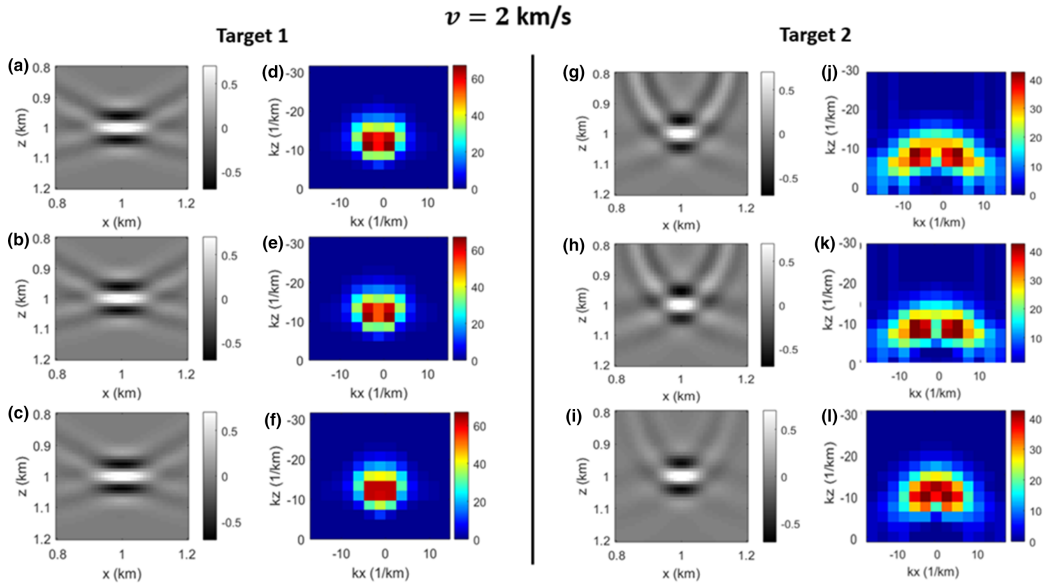


Figure 3 PSFs and wavenumber spectra for homogeneous velocity model with $v = 2$ km/s. (a–c) PSFs obtained from RTM, analytic implementation of equation (10) and analytic implementation of equation (16) for target 1. (d–f) Corresponding wavenumber spectra for the PSFs. (g–i) PSFs obtained from RTM, analytic implementation of equation (10) and analytic implementation of equation (16) for target 2. (j–l) Corresponding wavenumber spectra for the PSFs

survey parameters. Following the cross-correlation imaging condition inherent in RTM, an extra $|S(\omega)|$ factor was included in the numerator of Equation (16) to obtain the $|S(\omega)|^2$ term. All PSFs were further normalized to have a maximum amplitude of one to allow for relative comparison of the seismic responses. The PSFs, and their corresponding wavenumber spectra, are plotted in Figure 3 (low-velocity model) and Figure 4 (high-velocity model). Figure 5 illustrates a comparison of the centre traces obtained for all PSFs, both vertically and horizontally.

For target 1, all PSFs (Fig. 3a–c and Fig. 4a–c) have the same resolution patterns. The same observation applies in the corresponding wavenumber domains (Fig. 3d–f and Fig. 4d–f), where the spectra match in both overall coverage and in the amplitude range. We do, however, notice that the ray-based PSFs diverge slightly at the shallower target 2 (Figs 3i, 3l, 4i and 4l). This is further illustrated in Figure 5. Here, we notice how for target 1, the centre traces from the analytically computed PSFs align almost perfectly with the traces obtained from the PSF extracted from a complete migration. For target 2, we notice slightly more deviations between the ray-based PSF traces and the others, both in the vertical and horizon-

tal directions. This is particularly seen for the shallow PSFs computed in the high-velocity model (Fig. 5d and h).

To understand the observed differences, we consider Equations (10) and (16) again. First, we keep in mind that both equations are derived under a far-field approximation. Some deviations from the PSFs extracted from RTM are therefore to be expected for both approaches, particularly at the shallower target 2. To quantify this issue, we computed the PSF at 49 equidistant grid points in the low-velocity model using the Green's function defined in (8) with full Hankel functions rather than their asymptotic approximation. At all 49 targets, the absolute error spectra obtained from subtracting the PSFs obtained with the Green's function defined in (8) from the PSFs obtained under the far-field assumption in (10) were calculated. The standard deviation was then computed for each error spectrum, and 2D linear interpolation was applied to obtain expected standard deviation values for the entire model. Figure 6 illustrates the obtained result. We notice that the deviation is largest close to the shot point, as expected considering that the criteria $kR \gg 1$ might not be fulfilled here. We do, however, also notice that the standard deviation values are close to zero for most parts of the model, meaning that the

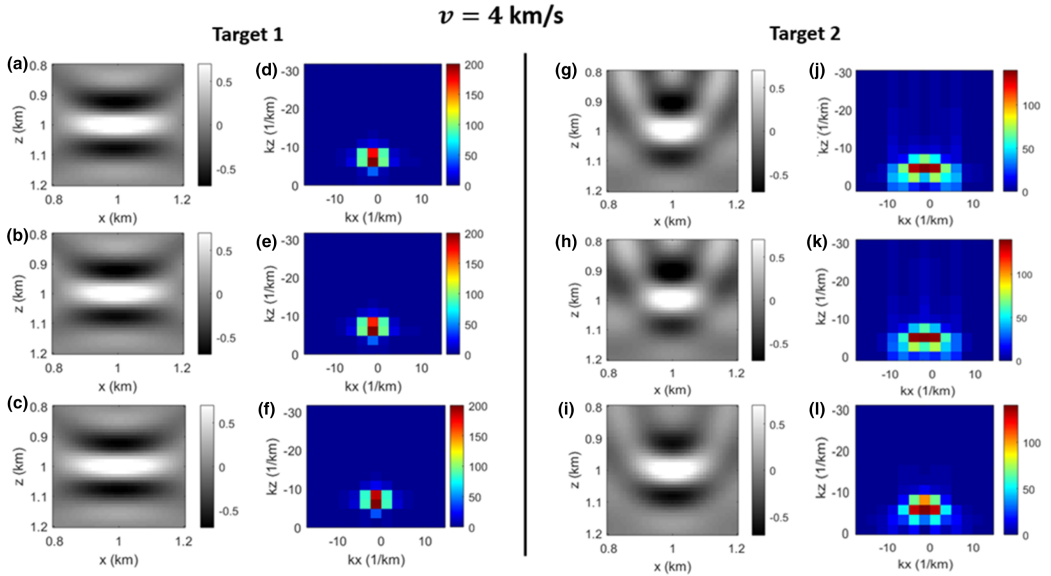


Figure 4 PSFs and wavenumber spectra for homogeneous velocity model with $v = 4$ km/s. (a–c) PSFs obtained from RTM, analytic implementation of equation (10) and analytic implementation of equation (16) for target 1. (d–f) Corresponding wavenumber spectra for the PSFs. (g–i) PSFs obtained from RTM, analytic implementation of equation (10) and analytic implementation of equation (16) for target 2. (j–l) Corresponding wavenumber spectra for the PSFs

far-field approximation should be valid throughout most of the model.

Regarding the two approaches themselves, we note that the phase terms are identical in both equations. Differences between the two approaches thus depend on the amplitude factors. We notice that in the ray approach, as expressed by (16), we only consider the distance to the image point at \mathbf{r} , in question, and not the surrounding scattering points located at \mathbf{r}' . In essence, the amplitude term in (16) may be considered as a simple scaling factor valid throughout the entire target of interest. This follows from (14) where we deconvolve the amplitude factors in accordance with the plane-wave assumption. The amplitude factors in (16) are therefore not attributable to the Green's functions, but merely result from the Jacobian mapping between the scattering wavenumber and acquisition domains.

We illustrate this effect by again considering the two targets in the low-velocity model. Using the analytical expression in (10), we computed the PSF amplitude responses (assuming a constant phase of value one) obtained at the point scatterers. For simplicity, we let $\omega = 1$ and set $|S(\omega)| = 1$ during the computations to extract amplitude variations only. By selecting the same PSF window of size $0.4 \text{ km} \times 0.4 \text{ km}$ and normalizing

the centre point of the PSFs to a value of one in both cases, we obtained the amplitude responses presented in Figure 7. The corresponding amplitude responses for the ray-based approach obtained via (16) would simply, following the plane-wave assumption, yield a constant value throughout the entire PSF window.

As amplitudes vary within the target area for the wave-based approach, slight asymmetry around the centre point along the high-resolution axis (in this case the vertical axis) is expected for traces obtained from the wave-based PSF. We also notice that the amplitude range is larger for the shallow target (Fig. 7b). This also follows from (10) as a smaller distance between shot point and target point yields smaller values for the \mathbf{r} and \mathbf{r}' parameters in the denominator in (10). The asymmetry is usually negligible if the PSF operator only spans a small amount of grid points around the centre point. However, for low-resolution PSFs resulting from low-frequency bandwidth, and/or high velocity at the target area, the effect would be more noticeable. This is for instance observed in Figures 4(h) and 5(d), where the combination of small distance between shot point and target point, high velocity, and low wavelet frequency, yields a noticeable asymmetry around the PSF centre point for the wave-based PSF. Furthermore, the plane-wave

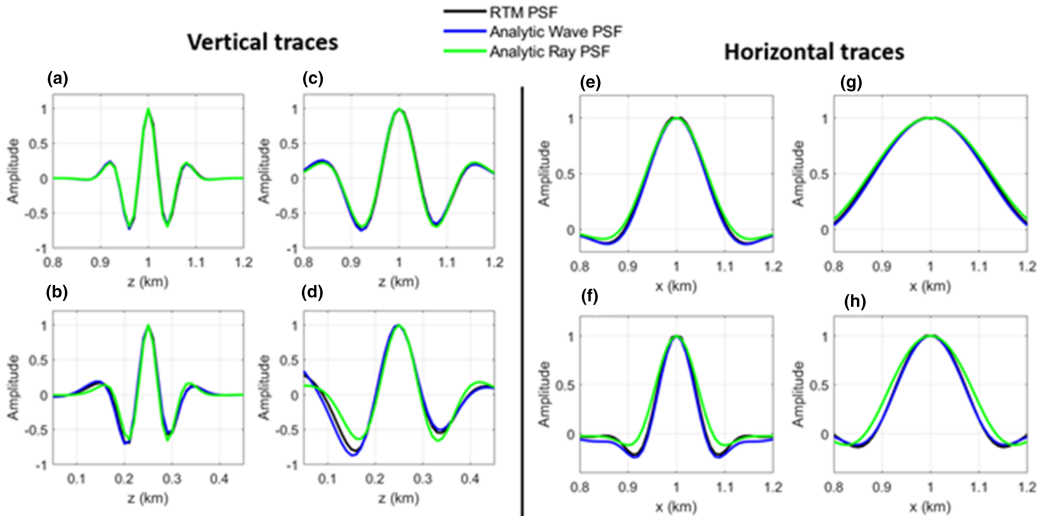


Figure 5 Left: Vertical centre traces obtained from PSFs at (a) target 1 ($v = 2$ km/s), (b) target 2 ($v = 2$ km/s), (c) target 1 ($v = 4$ km/s) and (d) target 2 ($v = 4$ km/s). Right: Horizontal centre traces obtained from PSFs at (e) target 1 ($v = 2$ km/s), (f) target 2 ($v = 2$ km/s), (g) target 1 ($v = 4$ km/s) and (h) target 2 ($v = 4$ km/s)

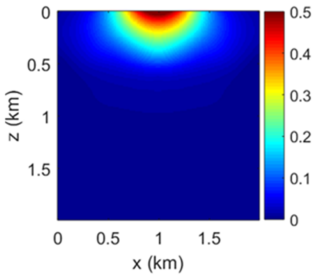


Figure 6 Standard deviation of absolute error spectra obtained between normalized PSFs estimated with and without the far-field approximation expressed in equation (9) at 49 equidistant points followed by 2D interpolation. The computations were performed in the homogeneous model with constant velocity of $v = 2$ km/s

assumption inherent in the far-field ray-based approach may produce differences in the PSF side lobes compared with wave-based PSFs where curvature effects are preserved. These effects should also be more prominent for shallow targets.

To illustrate in greater detail how the wave-generated PSFs may diverge from ray-generated PSFs in the homogeneous case, we estimated amplitude ranges as illustrated in Figure 7 for normalized PSFs obtained via (10) at 81 equidistant grid points in the low-velocity model. The stan-

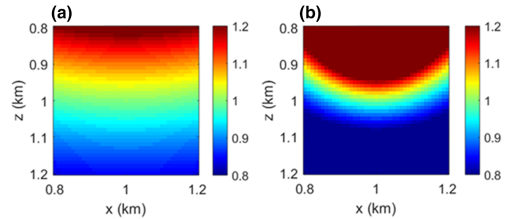


Figure 7 Normalized PSF amplitude responses obtained at (a) target 1 and (b) target 2 via Equation (10) in the homogeneous model with constant velocity of $v = 2$ km/s

dard deviation was then computed for each obtained amplitude range. Finally, 2D linear interpolation was applied to estimate expected standard deviation values for the entire velocity model. The obtained results are illustrated in Figure 8. The results confirm that the divergence between the two approaches will decrease with increasing distance from shot point in a homogeneous model.

In summary, divergence between wave-based and ray-based approaches is attributable to the ray-based local plane-wave assumption in amplitude, normalization with respect to reflectivity, the far-field approximation and the Jacobian mapping taking into account irregular sampling of the model space. The divergence is mostly observed for shallow targets

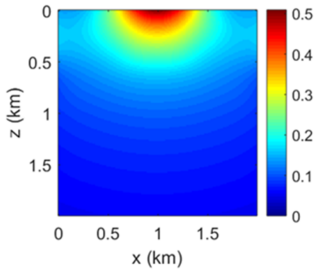


Figure 8 Standard deviation of normalized amplitude ranges obtained via equation (10) at targets sized 0.4×0.4 km estimated at 81 equidistant points followed by 2D interpolation. The computations were performed in the homogeneous model with constant velocity of $v = 2$ km/s

characterized by high-velocity and/or low-frequency bandwidth. However, as such a combination is, as pointed out, geologically unrealistic, we should, within the validity of ray theory and even for complex models, not expect much divergence between PSFs regardless of whether they are estimated with a wave- or ray-based approach.

ESTIMATING POINT-SPREAD FUNCTIONS IN INHOMOGENEOUS MODELS

In a homogeneous model, it is straightforward to analytically implement (10) and (16) and compute the seismic response due to a point scatterer. However, the Green's functions are not so easily computed for more complex models and must be estimated via other methods.

When applying a wave-based approach, one option is to estimate the PSFs by implementing the wave equation to retrieve the required Green's functions in (5). The true velocity model is then used for estimating the forward modelled Green's functions, and the—often smooth—migration velocity model is used for estimating the back-propagation (Xie *et al.*, 2005). An alternative approach is to perturbate the velocity or density value at a single point in the smooth velocity model, followed by forward modelling and migration over the model. The extracted point-scatterer response would then yield the PSF (Cao, 2013).

If a ray-based approach is implemented, we may, following Lecomte and Gelius (1998) and Lecomte (2008), estimate the scattering wavenumber vectors in (13) from ray tracing or similar (e.g. eikonal solvers) in a smooth background velocity model (as done in actual migration). First, a target point is selected for PSF computation. With a plane-wave assump-

tion, ray tracing is then used to calculate the incident and scattered slowness vectors (\mathbf{p}_S and \mathbf{p}_R) at the target point for each shot–receiver combination in a seismic survey. The so-called *illumination vectors*, $\mathbf{I}_{SR} = \mathbf{p}_R - \mathbf{p}_S$, are then computed for all these combinations (Fig. 9a). It can be shown mathematically that any reflector perpendicular to an illumination vector will be well illuminated (Gelius *et al.*, 2002a). As such, the fan of resulting illumination vectors obtained from all shot–receiver combinations in the survey (Fig. 9b) contains information about the local geological-dip range which may be imaged at the point of interest. Furthermore, the local cross-reflector resolution depends on the magnitude of each illumination vector, which is estimated as a function of opening angle and medium velocity via (Lecomte, 2008):

$$\mathbf{I}_{SR} = \frac{2 \cos\left(\frac{\theta_{SR}}{2}\right)}{c} \mathbf{u}_{SR}, \quad (17)$$

where θ_{SR} is the opening angle between the incident and scattered wavefield, c is the velocity of the incoming and scattered wavefields at the image point, and \mathbf{u}_{SR} is a unit vector pointing in the direction of \mathbf{I}_{SR} . By mapping the properly weighted wavelet spectrum (e.g. squared in the case of a cross-correlation imaging condition following equations (7) and (10)) along each illumination vector, scattering wavenumber vectors as defined in (13) are obtained for the target point (Fig. 9c). The entire collection of scattering wavenumber vectors now represents the PSF in the wavenumber domain. A Fourier transform of the spectrum yields the PSF in the space domain (Fig. 9d).

An important point to consider is that the procedure illustrated in Figure 9 assumes that the wavenumber spectrum is defined directly on a regular grid in the wavenumber domain. Intrinsically, however, scattering wavenumber vectors are best mapped in the polar domain in 2D (spherical in 3D). But a direct implementation of a 2D FFT in such a domain, followed by a polar-to-Cartesian transformation, is cumbersome because seismic data are typically characterized in the polar domain by very irregular sampling of the angular coordinate (corresponding to irregular – and possibly lacking – illumination). As such, various non-uniform interpolation and resampling strategies are used when converting raw data from polar coordinates to Cartesian coordinates. This is seen in, e.g., synthetic aperture radar (SAR) imaging (e.g. Carrara *et al.*, 1995; Jakowatz *et al.*, 1996; Doerry, 2012). Note, however, that the mentioned studies contain far less irregular sampling than in seismic data as these studies deal with a homogeneous background velocity field (i.e. the air).

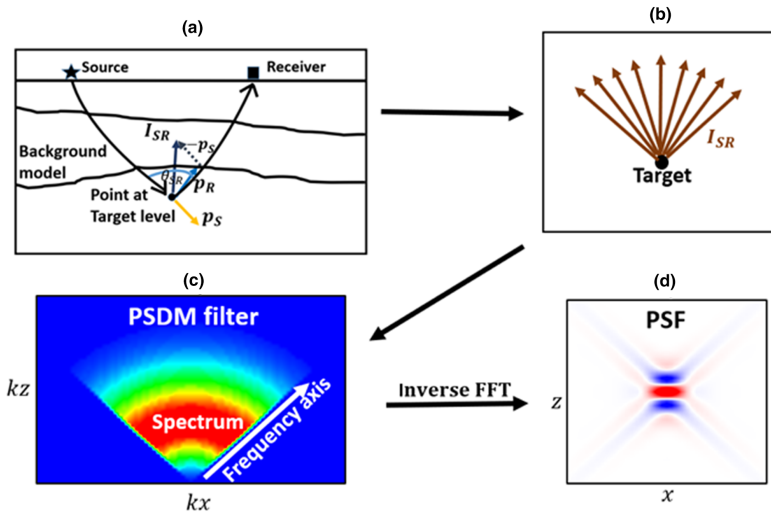


Figure 9 Procedure for estimating PSFs via ray-based approach. (a) Ray tracing is used to estimate the illumination vector (I_{SR}) for a single shot at a target point. (b) All illumination vectors for a complete survey are obtained. (c) Illumination vectors are combined with the wavelet frequency spectrum to obtain the local PSDM filter. (d) The PSF is obtained in the space ($x - z$) domain via an inverse Fourier transform

In our approach, a *nearest-point* interpolation technique is simply used. This technique is easy to implement and highly efficient: each polar sample is assigned to the nearest sample of the selected regular grid. However, such a mapping of points along vectors all attached to the same origin or pole (here, the reference point for which the PSF is calculated) yields an irregular hit count, i.e. with a higher number of hits close to the origin (where $K_x = K_z = 0$) than further away. To compensate for this effect, the value at each grid cell is normalized by dividing it with the number of hits at that cell (Lecomte *et al.*, 2005). This simple and efficient procedure both compensates for the polar-to-Cartesian mapping (Jacobian) and a possibly irregular illumination, including local redundancy leading to coherent noise in the migrated image (see example in Lecomte *et al.*, 2005; Fig. 16). The simulated prestack depth-migrated (PSDM) image obtained this way is, in essence, representing a ‘perfect’ PSDM image where the illumination has been regularized, as it should. If the goal, however, is to simulate PSDM images obtained from a migration algorithm with a different imaging condition which does not properly compensate for irregular illumination, in particular in the case of redundant illumination, the mapping may first be done directly in the polar domain, where one can easily control range and sampling while keeping the actual illumination hit. The final mapping over to the Cartesian domain could then be done by interpola-

tion after accounting for aliasing via, e.g., adequate smoothing (Lecomte *et al.*, 2005).

CASE STUDY: BP STATICS BENCHMARK MODEL

To assess the validity of simulated prestack depth-migrated (PSDM) images obtained via point-spread function (PSF) convolution modelling, we consider a slightly modified subsection of the 1994 BP Statics Benchmark P-velocity model (Ellison and Innanen, 2016). The velocity model is illustrated in Figure 10(a) with three selected target areas highlighted. The subsection is dominated by a large high-velocity intrusion in a complex geological setting characterized by uneven layers and faults. A thin, homogeneous water layer with constant P-velocity of 1.5 km/s was added on top of the model for simulation of a marine-type survey. Model and survey parameters are defined in the Figure 10 caption.

Using a zero-phase Ricker wavelet with a peak frequency of 20 Hz, sampled at 1 ms, finite-difference forward modelling was performed using the same approach as in the homogeneous case. Similarly, half-spaces were added at all four boundaries to avoid unwanted boundary reflections. Next, RTM was applied on the forward modelled traces. For the migration itself, a velocity model smoothed over slowness was

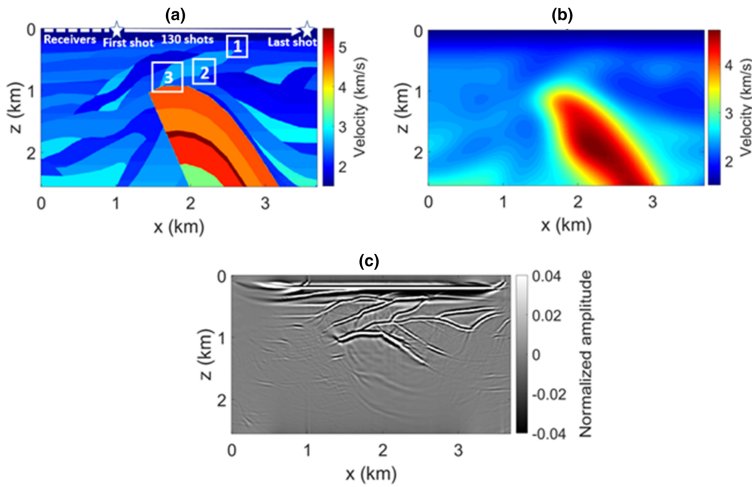


Figure 10 (a) P-velocity model and survey geometry with targets and survey parameters highlighted. The white boxes represent targets for PSF convolution modelling. (b) Smoothed P-velocity model. (c) Migrated image obtained from RTM. Size of subsection: 256×370 grid points. Sample interval: $dx = dz = 0.01$ km. Survey: marine-type. Survey depth: $z = 0.01$ km. First shot: $x = 0.99$ km. Last shot : $x = 3.57$ km. Number of shots: 130. Shot spacing: 0.02 km. Receiver array: 100 receivers spaced 0.01 km apart at depth $z = 0.01$. Initial receiver array from $x = 0$ km to $x = 0.99$ km. The receiver array moves 0.02 km between each shot

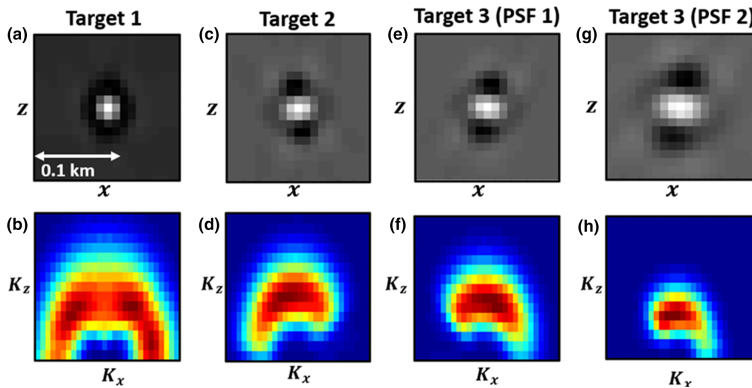


Figure 11 Wave-based PSFs and corresponding wavenumber spectra for PSFs generated at the targets highlighted with white boxes in Figure 10(a). Wavenumber spectra are plotted for K_x between -32.9 and $+32.9 \text{ km}^{-1}$, and for K_z between -37.8 and -3.7 km^{-1}

applied (Fig. 10b). The final image obtained after RTM is illustrated in Figure 10(c). A phase-shift operator was applied to the migrated traces to obtain approximate zero-phase traces.

Following the procedure in Cao (2013), wave-based PSFs were estimated at the centre of the three target areas by adding point scatterers to the smooth velocity model presented in Figure 10(b) and extracting their responses after forward modelling and RTM. All wave-based PSFs, with corresponding

wavenumber spectra, are illustrated in Figure 11. For target 3, an additional PSF was estimated just below the boundary of the high-velocity intrusion. This was done as targets characterized by high-velocity contrasts and complex geology may need to account for space-variant PSFs for accurate modelling results, as both the illumination and across-reflector resolution may vary substantially throughout the target area. For target 3, we therefore illustrate the different results obtained

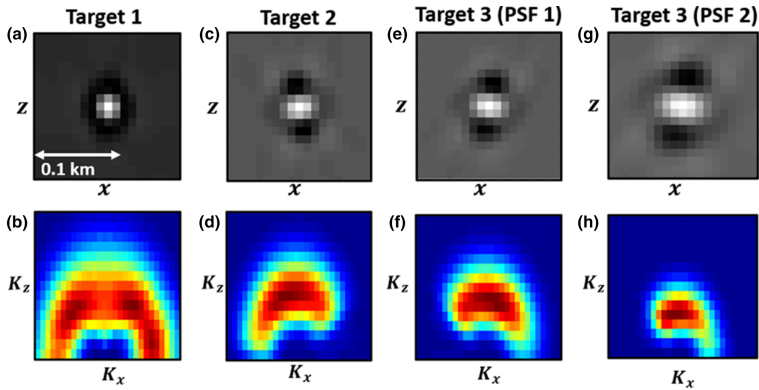


Figure 12 Ray-based PSFs and corresponding wavenumber spectra for PSFs generated at the targets highlighted with white boxes in Figure 10(a). Wavenumber spectra are plotted for K_x between -32.9 and $+32.9 \text{ km}^{-1}$, and for K_z between -37.8 and -3.7 km^{-1}

when employing a single PSF versus employing two PSFs. In the combined image, the centre PSF was convolved with the reflectivity grid above the high-velocity intrusion, and the other PSF was convolved with the reflectivity grid at and below the intrusion boundary. For simplicity, the two modelled images were then simply added together to yield the final image.

Using a wavefront construction approach presented in Vinje *et al.* (1993), ray tracing was next performed in the same smooth velocity model in order to estimate ray-based PSFs at the centre of each target area via the procedure outlined in Figure 9. For target 3, as we did for the wave-based approach, an additional PSF was estimated below the intrusion boundary. P-wave reflections were estimated based on the average reflectivity and average angle range values obtained from ray tracing. This was done for simplicity, as such an approach only requires one modelling run instead of multiple modelling runs for combination of angle ranges. All ray-based PSFs, with corresponding wavenumber spectra, are illustrated in Figure 12.

For each target, the seismic amplitude values were normalized by extracting the amplitude value from the same point at a well-imaged reflector and setting this value equal in the migrated and modelled images. The results obtained at all targets are illustrated in Figures 13–16. We will now discuss the overall findings with focus on how well the modelled images capture illumination, resolution and amplitude effects observed in the PSDM image.

Illumination effects

Targets 1 and 2 are located in well-illuminated parts of the model. The migrated results (Figs 13a and 14a) capture all the

geological features observed in the reflectivity grids (Figs 13b and Fig. 14b). We further observe that the modelled results (Fig. 13c–d and Fig. 14c–d) match the migrated results well. For target 2, however, there is a slight dimming of the modelled seismic response at the steepest part of the upper reflector (yellow box in Fig. 14c and d). By comparing the traces obtained at $x = 2.15 \text{ km}$ (Fig. 14e), we do observe in more detail how the amplitudes of the modelled traces weaken at depths around $z = 0.66 \text{ km} - 0.7 \text{ km}$ compared with the migrated trace. This could result from minor changes in illumination affecting different parts of the target area.

Illumination effects are also captured well by the modelled images for target 3, whether through the use of one PSF (Fig. 15) or two PSFs (Fig. 16). Target 3 is characterized by two primary reflectors, with a fault crossing the layer between the reflectors. The fault is not imaged in the migrated image (Fig. 15a) due to lack of illumination. This is also captured through PSF convolution modelling using both wave-based and ray-based PSFs (Fig. 15c–d and Fig. 16c–d). As such, this illustrates how PSF convolution modelling may properly account for limited illumination of dipping geological features such as faults, even when the latter have an elastic impedance contrast across.

Resolution effects

Differences in resolution between the migrated and modelled images are primarily observed at target 3, which is characterized by high-velocity contrasts. No discernible differences in resolution are observed for targets 1 and 2, but for target 1 we notice that the wave-based traces plotted in Figure 13(e, f)

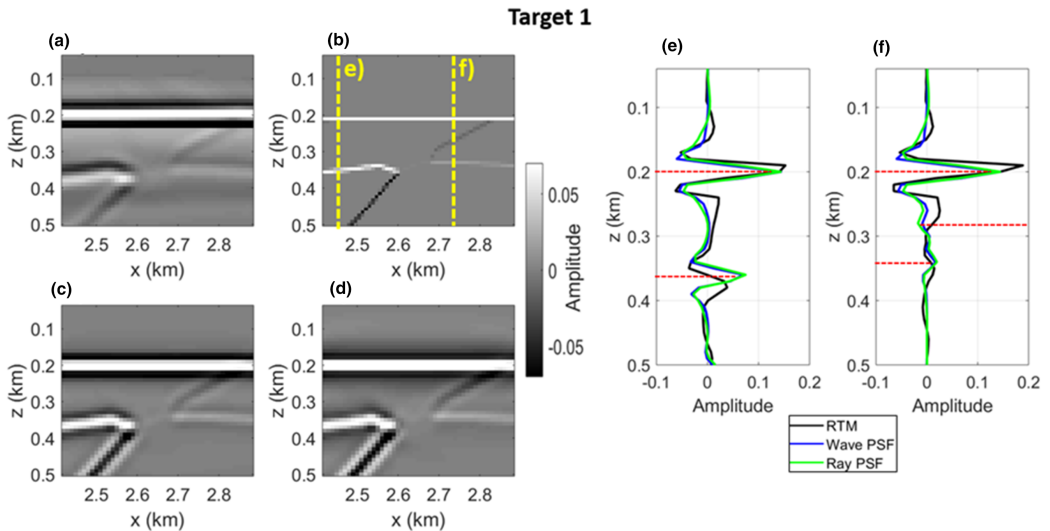


Figure 13 Results obtained for target 1 from (a) RTM; (b) input reflectivity grid; (c) wave-based PSF convolution modelling; (d) ray-based PSF convolution modelling. (e) Traces obtained at $x = 2.45$ km from migrated and modelled results (yellow line marked (e) in Fig. 13b). (f) Traces obtained at $x = 2.73$ km from migrated and modelled results (yellow line marked (f) in Fig. 13b). The horizontal dashed lines in (e) and (f) represent exact reflector positions

align slightly closer to the traces obtained from the migrated image than the ray-based traces do. As illustrated in Figure 8 for the homogeneous case, this might be a result of the shallowness of the target. The lack of curvature effects captured by the ray-based PSFs may also yield slightly different responses. At target 2, the traces obtained from wave-based and ray-based convolution (Fig. 14e, f) are almost identical and overall align better than for the shallower target 1, indicating that the greater target depth leads to less divergence between the wave-based and ray-based PSFs.

For target 3, however, we observe that the lower reflector, representing the intrusion boundary, suffers from slightly worse resolution in the migrated image (Fig. 15a) than in the modelled images (Fig. 15c–d). This is not surprising as the single PSFs used for convolution modelling in Figure 15(c, d) were estimated at the centre of the target area, located above the intrusion boundary. The lower velocity here yields PSFs with greater resolution than a PSF estimated at, or below, the boundary. By comparing traces extracted at $x = 1.61$ km (Fig. 15f), we do notice how the resolution of the migrated trace deviates from the modelled traces at the lower reflector. In order to mitigate this issue, multiple PSFs may be used to capture the spatial variability of the PSFs at the target. As illustrated in Figure 16(c, d), we indeed observe that when a sec-

ond PSF is estimated below the intrusion boundary and used for convolution with the lower part of the reflectivity grid, the combined image obtained from the two PSF convolutions better capture the resolution observed in the migrated image. This is also evident if we compare the traces plotted in Figure 16(f). What is of note is that the traces obtained from wave-based and ray-based PSFs overlap almost perfectly (Fig. 16e, f), indicating that both methods yield approximately identical results at this target.

Amplitude effects

The use of a single PSF convolution operator may, in some cases, not fully capture amplitude effects caused by transmission loss. For target 1, we notice that the loss of energy of the transmitted wave across the main reflector results in slightly greater amplitude contrast between the reflectors in the migrated image (Fig. 13a) compared with the modelled images (Fig. 13c–d). As the modelled images were obtained by convolving only one PSF with the input target reflectivity grid, this transmission effect is not accounted for. This is also observed in the traces obtained at $x = 2.45$ km (Fig. 13e). We observe here that the modelled traces, whether a wave-based or ray-based PSF is applied, indeed deviate slightly from the

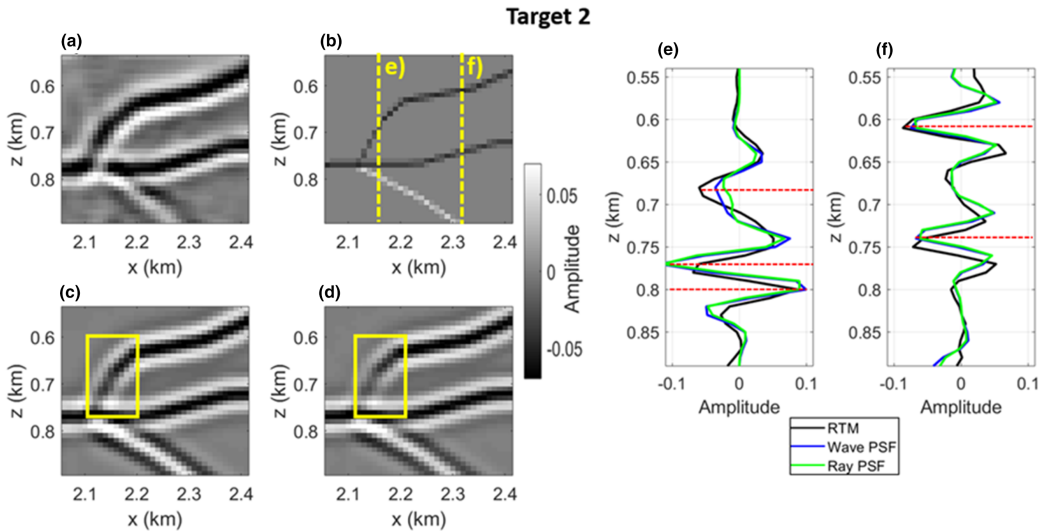


Figure 14 Results obtained for target 2 from (a) RTM; (b) input reflectivity grid; (c) wave-based PSF convolution modelling; (d) ray-based PSF convolution modelling. (e) Traces obtained at $x = 2.15$ km from migrated and modelled results (yellow line marked (c) in Fig. 14b). (f) Traces obtained at $x = 2.33$ km from migrated and modelled results (yellow line marked (f) in Fig. 14b). The horizontal dashed lines in (e) and (f) represent exact reflector positions

migrated trace in terms of amplitude. The same phenomenon is observed for target 3 and is particularly evident in the trace obtained at $x = 1.61$ km (Fig. 15f). When two PSFs are used, this problem is mitigated (Fig. 16f).

Amplitude differences between migrated and modelled images could also, in general, be caused by migration artefacts, interference issues and/or wave-energy originating from other parts of the model outside the considered target area. Such effects may not be fully captured by the (local) PSF convolution operators. The amplitude dimming observed in the part of target 2 highlighted by the yellow box in Figure 14(c, d) could, in addition to illumination sensitivity at the target, be explained by this phenomenon. Sharp boundaries in areas with high-velocity contrasts are prone to migration artefacts, and we do also notice for target 3 that the migrated image (Fig. 15a) appears to suffer from such artefacts at the diffraction point where the intrusion boundary begins to dip.

We further notice that, although most traces at all targets match well in terms of peak and trough locations, some deviations between the migrated and modelled traces are observed. Examples include the lower reflector in Fig. 14f (target 2) and the lower reflector in Figures 15(f) and 16(f) (target 3). This is most likely attributable to slight misalignments of reflector locations in the PSDM image, resulting from the

smoothing of the velocity model prior to back-propagation of the wavefield in the RTM algorithm.

DISCUSSION

The presented study illustrates the potential of target-oriented point-spread function (PSF) convolution modelling as a tool for simulating prestack depth-migrated (PSDM) images. For targets characterized by low-velocity contrasts, the use of one PSF estimated at the centre of the target area may be sufficient, thereby reducing computational cost. The cost may, however, still be significant if a wave-based approach is applied for PSF estimation. An alternative option is therefore to employ ray-based PSFs provided that the ray approach itself does not break down due to caustics, multipathing, etc. While the estimation of the wave-based PSFs in the BP Statics Benchmark Case required approximately ten hours of computation time on a standard workstation (3.40 GHz Intel core), the ray-based PSFs were estimated in approximately 20 seconds on the same workstation.

Our findings illustrate that images obtained through PSF convolution modelling, whether we apply a wave-based or ray-based PSF, accurately capture most illumination, resolution and amplitude effects observed in PSDM images.

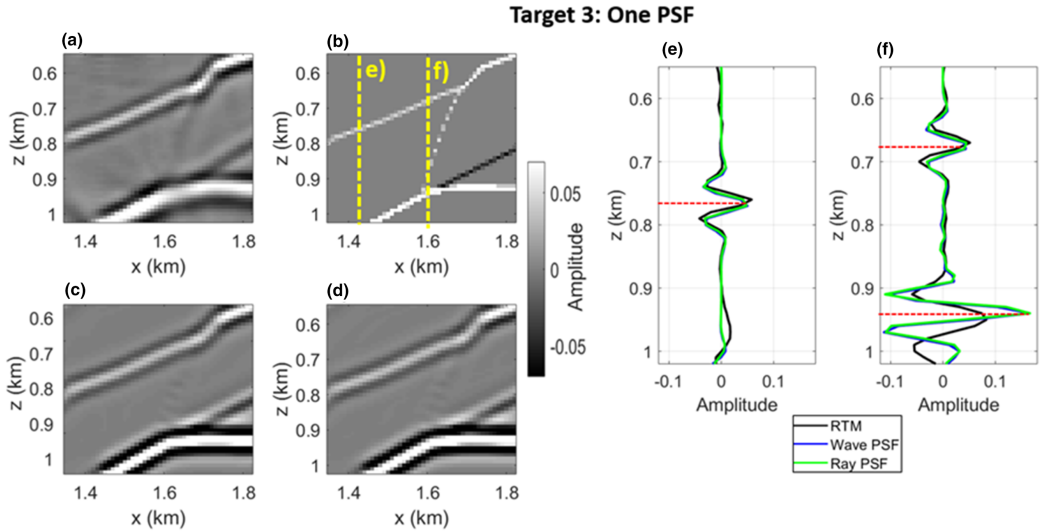


Figure 15 Results obtained for target 3 from (a) RTM; (b) input reflectivity grid; (c) wave-based PSF convolution modelling; (d) ray-based PSF convolution modelling. (e) Traces obtained at $x = 1.41$ km from migrated and modelled results (yellow line marked (e) in Fig. 15b). (f) Traces obtained at $x = 1.61$ km from migrated and modelled results (yellow line marked (f) in Fig. 15b). The horizontal dashed lines in (e) and (f) represent exact reflector positions

Amplitude effects such as migration artefacts, interference issues and wave-energy originating from outside a selected target area may, however, be challenging to capture. Future studies could assess possible approaches for capturing such effects in the PSF operators.

Regarding the PSF operators themselves, we observed that simulated PSDM images obtained via wave-based or ray-based PSFs were virtually indistinguishable for the applied synthetic models. The present study thus suggests that when PSF convolution modelling is applied for target-oriented seismic modelling, especially addressing the needs in, e.g. seismic interpretation, divergence effects between a wave-based and ray-based approach may be negligible. As such, ray-based PSFs may indeed offer an efficient and flexible alternative to wave-based PSFs given the very low computational cost involved. This is also confirmed from the analysis of the derived governing equations. However, as the derived equations only consider a 2D homogeneous isotropic medium, we acknowledge that further studies are required for more thorough assessments of how valid these findings are for complex cases. Furthermore, although the obtained results from the selected target areas of the BP Statics Benchmark model used in this study were found to be similar, other complex models with different geological challenges may yield greater divergence.

For more accurate seismic modelling, further refinements may be considered. One possibility is to include effects caused by anisotropy in the PSFs (Lecomte and Kaschwich, 2008). Another possibility is to include a more precise description on how the range of incidence angles impacts reflectivity, such as observed in amplitude versus offset (AVO)/amplitude versus angle (AVA) studies. Resolution of a target area of interest is determined by the combined effects of angle-dependent reflectivity and angle-dependent illumination/resolution (Lecomte, 2008). Future studies may therefore provide more accurate assessments of how the modelled amplitudes match migrated amplitudes without resorting to normalization, and which calibration strategies are most effective. Furthermore, the plane-wave assumption inherent in the ray-based PSF may be extended to a parabolic assumption to better capture curvature effects present in migrated images and wave-based PSFs (Gelius *et al.*, 2002b). For the near-field, higher-order paraxial ray theory could also be applied for more precise wavefront approximations. Yet another possibility is to design PSFs for elastic modelling with PS-converted waves. This extension is straightforward as it merely involves applying a scaling factor to the individual scattering wavenumber vectors in the wavenumber domain (Gelius *et al.*, 2002a). Such an approach could be useful to assess improvements in the imaging

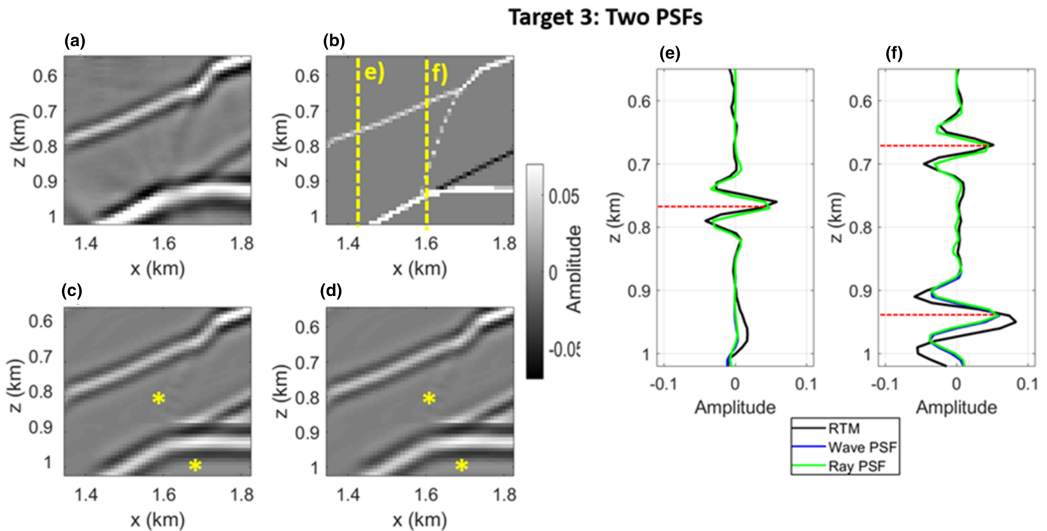


Figure 16 Results obtained for target 3 from (a) RTM; (b) input reflectivity grid; (c) wave-based PSF convolution modelling with PSFs, marked with stars, estimated at $(x, z) = (1.59 \text{ km}, 0.79 \text{ km})$ and $(x, z) = (1.67 \text{ km}, 1.01 \text{ km})$; (d) ray-based PSF convolution modelling with PSFs, marked with stars, estimated at same coordinates as in (c). (e) Traces obtained at $x = 1.41 \text{ km}$ from migrated and modelled results (yellow line marked (e) in Fig. 16b). (f) Traces obtained at $x = 1.61 \text{ km}$ from migrated and modelled results (yellow line marked (f) in Fig. 16b). The horizontal dashed lines in (e) and (f) represent exact reflector positions

of small-scale features, as the lower S-velocities would yield increased resolution, though the latter is often counterbalanced by higher attenuation effects.

Furthermore, the 2D PSF convolution approach analysed in this study is easily extendable to 3D models as well, with only a marginal increase in the computational cost. Several studies already document the potential of applying ray-based PSFs for simulating PSDM images of complex 3D geology (e.g. Lecomte, 2008; Lecomte *et al.*, 2015; Jensen *et al.*, 2021). Due to the reduced cost, simulation of 3D PSDM images may be obtained quickly on detailed models with significantly denser sampling than what FD approaches may allow. As such, flexible sensitivity studies of how various model parameters (geology, petrophysical properties) and seismic parameters (illumination, survey geometry etc.) affect seismic images may be performed. For this study, our limitation to simpler 2D models was motivated from our need to compare the ray-based results to results obtained via costly wave-based approaches. However, further validation studies aimed towards 3D migrated data should be a potential future area of study.

In addition to improving the validity of PSF convolution modelling as a forward modelling approach, the abovementioned suggestions for future studies can also improve the

application of PSFs as deconvolution operators. Even just a partial deconvolution of a migrated image may yield a substantial saving of computation time prior to, for instance, least-squares RTM (Aoki and Schuster, 2009). The speed in which ray-based PSFs can be designed may allow for efficient and flexible adjustments of the needed parameters, and further refinements are therefore desired for improved accuracy and validity. Overall, the choice of method is especially related to the application and data/method available. If one has full access to, and control of, the migration parameters, a wave-based PSF might be a better choice due to the guaranteed accuracy. However, when exact migration parameters are not available, ray-based approaches provide an easy, cheap and flexible alternative, providing one has a minimum of information about the velocity model and the migration needs.

CONCLUSIONS

Target-oriented point-spread functions (PSFs) used as spatial convolution operators allow for accurate seismic simulation of prestack depth-migrated (PSDM) images. Analytical modelling in a homogeneous velocity model based on governing equations derived for wave- and ray-based PSFs reveals

negligible differences between PSFs obtained via the two approaches for the homogeneous case. Further comparisons between PSF-convolved images and actual PSDM images obtained at selected targets in the BP Statics Benchmark model suggest that PSF convolution modelling accurately captures resolution, illumination and amplitude effects observed in migrated images. The results indicate that regardless of whether the PSFs are estimated through a wave-based or ray-based approach, the modelled results are usually virtually indistinguishable. Some minor divergence may, however, occur at targets characterized by close proximity between shot point and target point, high-velocity and/or low-frequency bandwidth, and at targets where the ray tracing algorithm may not fully account for amplitude and curvature effects. These effects may be primarily attributable to the far-field approximation inherent in ray theory. Further quantitative analyses of differences in PSDM images simulated via wave-based and ray-based PSFs should assess whether the former approach yields sufficient improvements to justify the increased cost.


ACKNOWLEDGEMENTS


The first author wishes to thank the University of Bergen for PhD project funding. Furthermore, the authors gratefully acknowledge NORSAR Innovation AS for providing an academic license of their modelling software. We acknowledge Amoco Tulsa Research Lab for developing and providing the BP Statics Benchmark model. We also thank Dr. Paul Lubrano-Lavadera for assistance in developing parts of our implemented computer codes. Finally, the authors would like to thank the Research Council of Norway for financial support through project #26763 (FOPAK).

DATA AVAILABILITY STATEMENT

The data that support the findings of this study are available from the corresponding author (first author) upon reasonable request.

ORCID

Kristian Jensen  <https://orcid.org/0000-0002-9002-6591>

Isabelle Lecomte  <https://orcid.org/0000-0002-3316-535X>

REFERENCES

Amini, H., MacBeth, C. and Shams, A. (2020) Seismic modelling for reservoir studies: a comparison between convolutional and full-

- waveform methods for a deep-water turbidite sandstone reservoir. *Geophysical Prospecting*, 68(5), 1540–1553. <https://doi.org/10.1111/1365-2478.12936>
- Aoki, N. and Schuster, G.T. (2009) Fast least-squares migration with a deblurring filter. *Geophysics*, 74(6), WCA83–WCA93. <https://doi.org/10.1190/1.3155162>
- Ayeni, G. and Biondi, B. (2010) Target-oriented joint least-squares migration/inversion of time-lapse seismic data sets. *Geophysics*, 75(3), R61–R73. <https://doi.org/10.1190/1.3427635>
- Beylkin, G., Oristaglio, M. and Miller, D. (1985) Spatial resolution of migration algorithms. In: A.J. Berkhout, J. Ridder and L.F. van der Waals, (Eds) *Proceedings of the 14th International Symposium on Acoustic Imaging*. Plenum Press, pp. 155–167.
- Bleistein, N., Cohen, J.K. and Stockwell Jr., J.W. (2001) *Mathematics of Multidimensional Seismic Imaging, Migration, and Inversion*. Springer, New York. <https://doi.org/10.1115/1.1399683>
- Botter, C., Cardozo, N., Hardy, S., Lecomte, I. and Escalona, A. (2014) From mechanical modeling to seismic imaging of faults: a synthetic workflow to study the impacts of faults on seismic. *Marine and Petroleum Geology*, 57, 187–207. <https://doi.org/10.1016/j.marpetgeo.2014.05.013>
- Botter, C., Cardozo, N., Qu, D., Tveranger, J. and Kolyukhin, D. (2017) Seismic characterization of fault facies models. *Interpretation*, 5(4), SP9–SP26. <https://doi.org/10.1190/INT-2016-0226.1>
- Cao, J. (2013) Resolution/illumination analysis and imaging compensation in 3D dip-azimuth domain. In: *83rd SEG Annual International Meeting, Houston, TX, USA*, Expanded Abstracts, pp. 3931–3936. <https://doi.org/10.1190/segam2013-0380.1>
- Carcione, J.M., Herman, G.C. and ten Kroode, A.P.E. (2002) Seismic modeling. *Geophysics*, 67(4), 1304–1325. <https://doi.org/10.1190/1.1500393>
- Carrara, W.G., Goodman, R.S. and Majewski, R.M. (1995) *Spotlight Synthetic Aperture Radar: Signal Processing Algorithms*. Artech House.
- Červený, V., Molotkov, I.A. and Pšenčík, I. (1977) *Ray method in seismology*. Charles University, Prague.
- Chen, J. and Schuster, G.T. (1999) Resolution limits of migrated images. *Geophysics*, 64(4), 1046–1053. <https://doi.org/10.1190/1.1444612>
- Claerbout, J.F. (1971) Toward a unified theory of reflector mapping. *Geophysics*, 36(3), 467–481. <https://doi.org/10.1190/1.1440185>
- Doerry, A. (2012) *Basics of Polar-Format Algorithm for Processing Synthetic Aperture Radar Images*. Sandia Report, pp. 1–66.
- Eide, C.H., Schofield, N., Lecomte, I., Buckley, S.J. and Howell, J.A. (2018) Seismic interpretation of sill complexes in sedimentary basins: Implications for the sub-sill imaging problem. *Journal of the Geological Society*, 175, 193–209. <https://doi.org/10.1144/jgs2017-096>
- Ellison, D.K. and Innanen, K. (2016) Improved resolution in depth imaging through reflection static corrections derived from model-based moveout. *Crewes Report*, 28, 1–12.
- Fehler, M., Huang, L., Wu, R.-S. and Xie, X.-B. (2005) Seismic image resolution: Numerical investigation of role of migration operator. In: *75th SEG Annual International Meeting, Houston, TX, USA*, Expanded Abstracts, P1870–P1873. <https://doi.org/10.1190/1.2148068>

- Gelius, L.-J. (1995) Generalized acoustic diffraction tomography. *Geophysical Prospecting*, 43(1), 3–29. <https://doi.org/10.1111/j.1365-2478.1995.tb00122.x>
- Gelius, L.-J., Johansen, I., Sponheim, N. and Stamnes, J.J. (1991) A generalized diffraction tomography algorithm. *The Journal of the Acoustical Society of America*, 89(2), 523–528. <https://doi.org/10.1121/1.400376>
- Gelius, L.-J., Lecomte, I. and Tabti, H. (2002a) Analysis of the resolution function in seismic prestack depth imaging. *Geophysical Prospecting*, 50(5), 505–515. <https://doi.org/10.1046/j.1365-2478.2002.00331.x>
- Gelius, L.-J., Lecomte, I. and Hamran, S.-E. (2002b) The concept of local parabolic-wave imaging (Lpl) in PSDM. In: *72nd SEG Annual International Meeting, Salt Lake City, UT, USA*, Expanded Abstracts, P1184–P1187. <https://doi.org/10.1190/1.1816862>
- Gjøystdal, H., Iversen, E., Lecomte, I., Kaschwich, T. and Drottning, Å.A.M., J. (2007) Improved applicability of ray tracing in seismic acquisition, imaging, and interpretation. *Geophysics*, 72(5), SM261–SM271. <https://doi.org/10.1190/1.2736515>
- Grippa, A., Hurst, A., Palladino, G., Iacopini, D., Lecomte, I. and Huuse, M. (2019) Seismic imaging of complex geometry: forward modeling of sandstone intrusions. *Earth and Planetary Science Letters*, 513, 51–63. <https://doi.org/10.1016/j.epsl.2019.02.011>
- Guitton, A. (2004) Amplitude and kinematic corrections of migrated images for nonunitary imaging operators. *Geophysics*, 69(4), 1017–1024. <https://doi.org/10.1190/1.1778244>
- Hamran, S.-E. and Lecomte, I. (1993) Local plane-wavenumber diffraction tomography in heterogeneous backgrounds. Part 1: Theory. *Journal of Seismic Exploration*, 2, 133–146.
- Jakowatz, C.V. Jr., Wahl, D.E., Eichel, P.H., Ghiglia, D.C. and Thompson, P.A. (1996) *Spotlight-Mode Synthetic Aperture Radar: A Signal Processing Approach*. Kluwer Academic Publishers.
- Jensen, K., Johansen, M.K., Lecomte, I., Janson, X., Tveranger, J. and Kaschwich, T. (2021) Paleokarst reservoirs: efficient and flexible characterization using point-spread-function-based convolution modeling. *Interpretation*, 9(2), T331–T347. <https://doi.org/10.1190/INT-2020-0130.1>
- Jensen, K., Lecomte, I. and Kaschwich, T. (2018) Analyzing PSDM images in complex geology via ray-based PSF convolution modeling. In: *88th SEG Annual International Meeting, Anaheim, CA, USA*, Expanded Abstracts, pp. P3843–P3847. <https://doi.org/10.1190/segam2018-2995975.1>
- Jiang, B. and Zhang, J. (2019) Least-squares migration with a blockwise Hessian matrix: a prestack time-migration approach. *Geophysics*, 84(4), R625–R640. <https://doi.org/10.1190/geo2018-0533.1>
- Kjøberg, S., Schmiedel, T., Planke, S., Svensen, H.H., Millett, J.M., Jeram, D.A., et al. (2017) 3D structure and formation of hydrothermal vent complexes at the Paleocene-Eocene transition, the Møre Basin, mid-Norwegian margin. *Interpretation*, 5(3), SK65–SK81. <https://doi.org/10.1190/INT-2016-0159.1>
- Lecerf, D. and Bessellievre, M. (2018) A new approach to compensate for illumination differences in 4D surveys with different individual acquisition geometries. *First Break*, 36, 71–76. <https://doi.org/10.3997/1365-2397.n0073>
- Lecomte, I. (2008) Resolution and illumination analyses in PSDM: a ray-based approach. *The Leading Edge*, 27, 650–663. <https://doi.org/10.1190/1.2919584>
- Lecomte, I. and Gelius, L.-J. (1998) Have a look at the resolution of prestack depth migration for any model, survey and wavefields. In: *68th SEG Annual International Meeting, New Orleans, LA, USA*, Expanded Abstracts, pp. P1112–P1115. <https://doi.org/10.1190/1.1820082>
- Lecomte, I., Gjøystdal, H. and Drottning, Å. (2003) Simulated prestack local imaging: a robust and efficient interpretation tool to control illumination, resolution, and time-lapse properties of reservoirs. In: *73rd SEG Annual International Meeting, Dallas, TX, USA*, Expanded Abstracts, pp. P1525–P1528. <https://doi.org/10.1190/1.1817585>
- Lecomte, I., Hamran, S.-E. and Gelius, L.-J. (2005) Improving Kirchhoff migration with repeated local plane-wave imaging? A SAR-inspired signal-processing approach in prestack depth imaging. *Geophysical Prospecting*, 53(6), 767–785. <https://doi.org/10.1111/j.1365-2478.2005.00501.x>
- Lecomte, I. and Kaschwich, T. (2008) Closer to real earth in reservoir characterization: a 3D isotropic/anisotropic PSDM simulator. In: *78th SEG Annual International Meeting, Las Vegas, NV, USA*, Expanded Abstracts, pp. P1570–P1574. <https://doi.org/10.1190/1.3059213>
- Lecomte, I., Lavadera, P.L., Anell, I., Buckley, S.J., Schmid, D.W. and Heeremans, M. (2015) Ray-based seismic modeling of geological models: Understanding and analyzing seismic images efficiently. *Interpretation*, 3(4), SAC71–SAC89. <https://doi.org/10.1190/INT-2015-0061.1>
- Lecomte, I., Lubrano-Lavadera, P., Botter, C., Anell, I., Buckley, S.J., Eide, C.H., et al. (2016) 2(3)D convolution modelling of complex geological targets – beyond 1D convolution. *First Break*, 34, 99–107. <https://doi.org/10.3997/1365-2397.34.5.84451>
- Lubrano-Lavadera, P., Senger, K., Lecomte, I., Mulrooney, M.J. and Kühn, D. (2019) Seismic modelling of metre-scale normal faults at a reservoir-cap interface in Central Spitsbergen, Svalbard: implications for CO₂ storage. *Norwegian Journal of Geology*, 99(2), 329–347. <https://doi.org/10.17850/njg003>
- Rabbel, O., Galland, O., Mair, K., Lecomte, I., Senger, K., Spacapan, J.B. and Manceda, R. (2018) From field analogues to realistic seismic modelling: a case study of an oil-producing andesitic sill complex in the Neuquén Basin, Argentina. *Journal of the Geological Society*, 175(4), 580–593. <https://doi.org/10.1144/jgs2017-116>
- Ristow, D. and Rühl, T. (1994) Fourier finite-difference migration. *Geophysics*, 59(12), 1882–1893. <https://doi.org/10.1190/1.1443575>
- Schuster, G.T. (2017) *Seismic Inversion*. Society of Exploration Geophysicists. <https://doi.org/10.1190/1.9781560803423>
- Schuster, G.T. and Hu, J. (2000) Green's function for migration: continuous recording geometry. *Geophysics*, 65(1), 167–175. <https://doi.org/10.1190/1.1444707>
- Sjøberg, T.A., Gelius, L.-J. and Lecomte, I. (2003) 2-D deconvolution of seismic image blur. In: *73rd SEG Annual International Meeting, Dallas, TX, USA*, Expanded Abstracts, P1055–P1059. <https://doi.org/10.1190/1.1817453>

- Tang, Y. (2009) Target-oriented wave-equation least-squares migration/inversion with phase-encoded Hessian. *Geophysics*, 74(6), WCA95–WCA107. <https://doi.org/10.1190/1.3204768>
- Thomson, C.J., Kitchenside, P.W. and Fletcher, R.P. (2016) Theory of reflectivity blurring in seismic depth imaging. *Geophysical Journal International*, 205(2), 837–855. <https://doi.org/10.1093/gji/ggw025>
- Thorbecke, J., Wapenaar, K. and Swinnen, G. (2004) Design of one-way wavefield extrapolation operators, using smooth functions in WLSQ optimization. *Geophysics*, 69(4), 1037–1045. <https://doi.org/10.1190/1.1778246>
- Toxopeus, G., Petersen, S. and Wapenaar, K. (2003) Improving geological modeling and interpretation by simulated migrated seismics. In: *65th EAGE Annual Conference and Exhibition, Stavanger, Norway*, Expanded Abstracts, F34. <https://doi.org/10.3997/2214-4609-pdb.6.F34>
- Toxopeus, G., Thorbecke, J., Wapenaar, K., Petersen, S., Slob, E. and Fokkema, J. (2008) Simulating migrated and inverted seismic data by filtering a geologic model. *Geophysics*, 73(2), T1–T10. <https://doi.org/10.1190/1.2827875>
- Valenciano, A.A., Biondi, B. and Guitton, A. (2006) Target-oriented wave-equation inversion. *Geophysics*, 71(4), A35–A38. <https://doi.org/10.1190/1.2213359>
- Vinje, V., Iversen, E. and Gjøystdal, H. (1993) Traveltime and amplitude estimation using wavefront construction. *Geophysics*, 58(8), 1157–1166. <https://doi.org/10.1190/1.1443499>
- Xie, X.-B., Wu, R.-S., Fehler, M. and Huang, L. (2005) Seismic resolution and illumination: a wave-equation based analysis. In: *75th SEG Annual International Meeting*, Houston, TX, USA, Expanded Abstracts, P1862–P1865. <https://doi.org/10.1190/1.2148066>
- Youzwishen, C.F. and Margrave, G.F. (1999) Finite difference modelling of acoustic waves in Matlab. *Crewe's Report*, 11, 1–19.
- Yu, J., Hu, J., Schuster, G.T. and Estill, R. (2006) Prestack migration deconvolution. *Geophysics*, 71(2), S53–S62. <https://doi.org/10.1190/1.2187783>
- Zhao, Z. and Sen, M. (2018) Fast image-domain target-oriented least-squares reverse time migration. *Geophysics*, 83(6), A81–A86. <https://doi.org/10.1190/1.2187783>

APPENDIX

In this appendix, we provide more details of the derivation of (15) and (16). Our starting point is equation (5) for the wave-based approach:

$$\text{PSF}_{\text{wave}}(\mathbf{r}|\mathbf{r}') = \int_{\omega} \int_{\mathbf{r}_g} \omega^4 |S(\omega)|^2 G(\omega, \mathbf{r}_g|\mathbf{r})^* G(\omega, \mathbf{r}|\mathbf{r}_s)^* G(\omega, \mathbf{r}'|\mathbf{r}_s) d\mathbf{r}_g d\omega. \quad (\text{A1})$$

For the ray-based approach, we introduce the high-frequency approximation of the Green's function defined in (11):

$$G(\omega, \mathbf{r}_j|\mathbf{r}) = A(\omega, \mathbf{r}_j|\mathbf{r}) \exp[i\omega\tau(\mathbf{r}_j|\mathbf{r})], \quad j = s, g. \quad (\text{A2})$$

Expanding the Green's function as a Taylor series around the reference point \mathbf{r}' , we obtain, following (12) and derived from a constant amplitude and a linear phase assumption within the local volume V_0 :

$$\begin{aligned} G(\omega, \mathbf{r}_g|\mathbf{r}') &\cong G(\omega, \mathbf{r}_g|\mathbf{r}) \cdot \exp[i\omega\nabla\tau(\mathbf{r}_g|\mathbf{r}) \cdot (\mathbf{r}' - \mathbf{r})] \\ G(\omega, \mathbf{r}'|\mathbf{r}_s) &\cong G(\omega, \mathbf{r}|\mathbf{r}_s) \cdot \exp[i\omega\nabla\tau(\mathbf{r}|\mathbf{r}_s) \cdot (\mathbf{r}' - \mathbf{r})]. \end{aligned} \quad (\text{A3})$$

Using the definition of the wavenumber vector in (13), and inserting (A3) in (A1) yields

$$\begin{aligned} \text{PSF}_{\text{ray}}(\mathbf{r}|\mathbf{r}') &= \int_{\omega} \int_{\mathbf{r}_g} \omega^4 |S(\omega)|^2 G(\omega, \mathbf{r}_g|\mathbf{r})^* G(\omega, \mathbf{r}|\mathbf{r}_s)^* \\ &G(\omega, \mathbf{r}_g|\mathbf{r}) G(\omega, \mathbf{r}|\mathbf{r}_s) \exp[i\mathbf{K} \cdot (\mathbf{r} - \mathbf{r}')] d\mathbf{r}_g d\omega. \end{aligned} \quad (\text{A4})$$

From (6) and (9), we see that the phase terms will cancel out in the analytical Green's functions for both 3D and 2D media when multiplied, leaving us with the amplitude terms:

$$\begin{aligned} \text{PSF}_{\text{ray}}(\mathbf{r}|\mathbf{r}') &= \int_{\omega} \int_{\mathbf{r}_g} \omega^4 |S(\omega)|^2 A(\omega, \mathbf{r}_g|\mathbf{r})^* A(\omega, \mathbf{r}|\mathbf{r}_s)^* \\ &A(\omega, \mathbf{r}_g|\mathbf{r}) A(\omega, \mathbf{r}|\mathbf{r}_s) \exp[i\mathbf{K} \cdot (\mathbf{r} - \mathbf{r}')] d\mathbf{r}_g d\omega. \end{aligned} \quad (\text{A5})$$

Using the complex conjugate relation $AA^* = |A|^2$, we get

$$\begin{aligned} \text{PSF}_{\text{ray}}(\mathbf{r}|\mathbf{r}') &= \int_{\omega} \int_{\mathbf{r}_g} \omega^4 |S(\omega)|^2 |A(\omega, \mathbf{r}_g|\mathbf{r})|^2 |A(\omega, \mathbf{r}|\mathbf{r}_s)|^2 \\ &\times \exp[i\mathbf{K} \cdot (\mathbf{r} - \mathbf{r}')] d\mathbf{r}_g d\omega. \end{aligned} \quad (\text{A6})$$

This represents the ray-based approach under the assumption of an adjoint operator given by \mathbf{L}^T . From (14), we may, at this point, under the assumption that the wavefield phase varies significantly faster than the wavefield amplitude within the local volume of interest, and that the PSF is normalized with respect to reflectivity, apply a more accurate approximation of the inverse \mathbf{L} operator (Gelius *et al.*, 1991; Gelius, 1995):

$$\mathbf{L}^{-1} = \frac{J[\mathbf{K}|\omega, \mathbf{r}_g]}{\omega^4 |S(\omega)| |A_s|^2 |A_g|^2} \mathbf{L}^T. \quad (\text{A7})$$

Inserted in (A6), this yields expression (15) in the main body of the paper:

$$\text{PSF}_{\text{ray}}(\mathbf{r}|\mathbf{r}') = \int_{\mathbf{K}} |S(\omega)| \exp[i\mathbf{K} \cdot (\mathbf{r} - \mathbf{r}')] d\mathbf{K}, \quad (\text{A8})$$

where $d\mathbf{K} = J(\mathbf{K}|\omega, \mathbf{r}_g) d\omega d\mathbf{r}_g$ is the Jacobian that maps between the Fourier-transformed model (scattering wavenumber) and the acquisition domain as illustrated in Figure 1.

In order to obtain (16) valid for a homogeneous 2D medium, we may first rewrite (A8):

$$\text{PSF}_{\text{ray}}(r|\mathbf{r}') = \int_{\mathbf{K}} |S(\omega)| \times \exp \left[\frac{i\omega}{c_0} (R_s(\mathbf{r}) + R_g(\mathbf{r}) - R_s(\mathbf{r}') - R_g(\mathbf{r}')) \right] d\mathbf{K}. \quad (\text{A9})$$

We now define

$$\phi(\mathbf{r}_s, \mathbf{r}_g, \mathbf{r}) = \frac{\omega}{c_0} [R_s(\mathbf{r}) + R_g(\mathbf{r})]. \quad (\text{A10})$$

To retrieve the solution in the acquisition domain for a single shot, we apply the Jacobian transform $d\mathbf{K} = J(\mathbf{K}|\omega, x_g)d\omega dx_g$, where from (13) and (A10) we obtain

$$J(\mathbf{K}|\omega, x_g) = \omega \begin{vmatrix} \frac{\partial^2 \phi}{\partial x \partial \omega} & \frac{\partial^2 \phi}{\partial z \partial \omega} \\ \frac{\partial x \partial \omega}{\partial x \partial x_g} & \frac{\partial z \partial \omega}{\partial z \partial x_g} \end{vmatrix}. \quad (\text{A11})$$

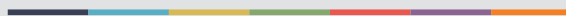
The computed Jacobian then becomes, using (A10), (A11) and the parameters from Figure 1:

$$J(\mathbf{K}|\omega, x_g) = \frac{\omega^2 |(z - z_g)(x - x_g)| |(x - x_s)R_g(\mathbf{r}) - (x_g - x)R_s(\mathbf{r})|}{c_0^2 R_s(\mathbf{r}) \cdot R_g(\mathbf{r})^4} + \frac{\omega^2 (z - z_g)^2 \cdot |(z - z_s)R_g(\mathbf{r}) - (z_g - z)R_s(\mathbf{r})|}{c_0^2 R_s(\mathbf{r}) \cdot R_g(\mathbf{r})^4} \quad (\text{A12})$$

Inserting into (A9) then finally yields the analytical solution expressed in (16).



Graphic design: Communication Division, UIB / Print: Skjipes Kommunikasjon AS



uib.no

ISBN: 9788230851821 (print)
9788230845790 (PDF)